

---


Electronic Theses and Dissertations, 2004-2019

---

2013

## Femtosecond Filament Interaction As A Probe For Molecular Alignment

Erik McKee  
*University of Central Florida*

 Part of the [Electromagnetics and Photonics Commons](#), and the [Optics Commons](#)  
Find similar works at: <https://stars.library.ucf.edu/etd>  
University of Central Florida Libraries <http://library.ucf.edu>

This Masters Thesis (Open Access) is brought to you for free and open access by STARS. It has been accepted for inclusion in Electronic Theses and Dissertations, 2004-2019 by an authorized administrator of STARS. For more information, please contact [STARS@ucf.edu](mailto:STARS@ucf.edu).

---

### STARS Citation

McKee, Erik, "Femtosecond Filament Interaction As A Probe For Molecular Alignment" (2013). *Electronic Theses and Dissertations, 2004-2019*. 2769.  
<https://stars.library.ucf.edu/etd/2769>

FEMTOSECOND FILAMENT INTERACTION AS A  
PROBE FOR MOLECULAR ALIGNMENT

by

ERIK MCKEE  
B.S. University of Central Florida, 2012

A thesis submitted in partial fulfillment of the requirements  
for the degree of Master of Science  
in the Department of Optics  
in the College of Optics and Photonics  
at the University of Central Florida  
Orlando, Florida

Fall Term  
2013

Major Professor: Martin Richardson

©2013 Erik McKee

## ABSTRACT

Femtosecond laser filamentation is a highly nonlinear propagation mode. When a laser pulse propagates with a peak power exceeding a critical value  $P_{cr}$  (5 GW at 800 nm in air), the Kerr effect tends to collapse the beam until the intensity is high enough to ionize the medium, giving rise to plasma defocusing. A dynamic competition between these two effects takes place leaving a thin and weakly ionized plasma channel in the trail of the pulse.

When an ultrafast laser pulse interacts with molecules, it will align them, spinning them about their axis of polarization. As the quantum rotational wave packet relaxes, the molecules will experience periodic field-free alignment. Recent work has demonstrated the effect of molecular alignment on laser filamentation of ultra-short pulses. Revival of the molecular alignment can modify filamentation parameters as it can locally modify the refractive index and the ionization rate. In this thesis, we demonstrate with simulations and experiments that these changes in the filament parameters (collapse distance and filament plasma length) can be used to probe molecular alignment in CO<sub>2</sub>.

## ACKNOWLEDGMENTS

I would like to acknowledge the guidance and support of my advisor, Dr. Martin Richardson. I am grateful for the opportunities, which without him would not have been possible. I would also like to thank Dr. Zenghu Chang and Dr. Matthieu Baudelet for being on my committee.

Dr. Tamar Seideman and Dr. Sai Ramakrishna have been fundamental to this research. Their expert knowledge and simulations on molecular alignment was essential to this work. Thank you both for all of your hard work on this project.

Outside of being a committee member, Dr. Matthieu Baudelet has been a great source of inspiration and motivation. He provided many powerful insights to my understanding of many topics, spanning spectroscopy, to plasma, to quantum mechanics. I am proud to have worked with him and have him on my committee.

I would like to thank Dr. Magali Durand for her guidance and mentoring. She was always there to support me in whatever way she could. She has been a monumental component for my success at CREOL. I wish her only the best in all of her future endeavors.

Dr. Larry Shah is an expert in finding solutions in the lab. His time spent working in the trenches of research with me was priceless. He seemed to always know some little trick to solve any problem. Thank you for all of your help throughout the years.

I would like to thank Dr. Pieter Kik for the many hour long conversations in his office. During my graduate studies at CREOL, he was more than willing to entertain and explore any of my ideas or proposals. His ability to pass knowledge to his students has raised the standard that

I judge professors. He has been an inspiration for me to innovate and pursue concepts that others may have discouraged.

Khan Lim has been the best lab partner/office mate. His skills have been instrumental to not only my research, but also to most of the research in the filamentation team. He has always been more than willing to take time out of whatever he was doing to answer my numerous questions.

I would like to thank my good friend Josh Bradford, my first mentor at CREOL back when I was in the REU program as an undergrad. He was the first person to introduce me to real work in a research lab. The time spent in lab with him laid the foundation for future research. I am grateful for the many hours spent with him.

Having Alex Sincore in most of my classes and in my group has been awesome. Spending time with him in or outside of CREOL to unwind has been filled with many great experiences. Many of the times with him will be remembered as highlights of my time in graduate school.

I would like to thank my girlfriend, Deanna Barnes. Without her, this thesis would not have been possible. She has dealt with all of my ups and downs as a graduate student. She would join me at the gym to pump iron regardless of the time of day, which allowed me to get out built-up stress.

Also, I would like to thank all of the current and former members of LPL that I have had the great pleasure of interacting with, Dr. Nick Barbieri, Dr. Mark Ramme, Dr. Matt Weidman, Dr. Andreas Vaupel, Dr. Christina Willis, Dr. Ilya Mingareev, Nathan Bodnar, John Szilagy, Ben Webb, Martin Gebhardt, Yuseong Jang, CheonHa Jeon, Andreas Knebl, Michael Muller, and Sy Wei Lew. I would like to thank everyone else at CREOL that has been influential to me.

Finally, I would like to thank all of my friends and family. Without their support I wouldn't have been able to overcome the obstacles to get where I am today.

## TABLE OF CONTENTS

LIST OF FIGURES.....	ix
LIST OF ACRONYMS.....	xii
1 INTRODUCTION .....	1
2 FILAMENTATION .....	3
2.1 Introduction .....	3
2.2 Ultrashort High Intensity Pulse Generation .....	4
2.2.1 Mode-locking.....	4
2.2.2 Chirped Pulse Amplification .....	5
2.3 Physics of Filamentation .....	5
2.3.1 Kerr Self-Focusing .....	6
2.3.2 Plasma Defocusing.....	6
2.3.3 Multiple Filaments.....	8
2.3.4 Continuum Generation with Filamentation .....	10
2.3.5 THz Generation.....	12
2.3.6 Guiding with Filamentation .....	14
3 MOLECULAR ALIGNMENT .....	17
3.1 Introduction.....	17
3.2 Static Field Alignment .....	25
3.3 Adiabatic Alignment.....	26
3.4 Non-adiabatic Alignment .....	29
3.5 Experimental Methods and Applications.....	32
4 EXPERIMENTAL SET-UP .....	39
4.1 Equipment .....	39
4.1.1 Laser.....	39
4.1.2 Gas Chamber .....	40
4.2 Data Collection .....	42
4.2.1 Pump-Probe Technique .....	42
4.2.2 Observables Measured.....	44
5 FILAMENT INTERACTION WITH ALIGNED CO <sub>2</sub> MOLECULES .....	46
5.1 Introduction and Motivation.....	46



5.2 Theoretical Studies.....	47
5.2.1 Laser Intensity dependence .....	50
5.2.2 Pressure Dependence.....	53
5.3 Experimental Results.....	54
5.3.1 Filament interaction with an aligned medium .....	54
5.4 Discussion .....	58
5.4.1 Population Decay and Coherence .....	62
5.5 Conclusion .....	65
6 CONCLUSION .....	67
6.1 Outlook and Future Work .....	68
APPENDIX: PULSE MEASUREMENT TECHNIQUES.....	70
LIST OF REFERENCES .....	76

## LIST OF FIGURES

Figure 1 Filamentation propagation dynamics.....	8
Figure 2 Conical emission from filament propagation in the normal dispersion regime [M. Durand 2011] .....	11
Figure 3. Two-color filament for THz generation setup [J. Dai 2010].....	13
Figure 4. Raw image by S. B. Leonov et al. (2012) of filamentation induced high voltage electrical discharge.....	16
Figure 5. Typical energy levels of a diatomic molecule. ....	17
Figure 6. Rotational spectrum of CO at 300 K [S. Mackenzie 2012].....	18
Figure 7. Relevant time scales for molecules .....	20
Figure 8. The angle $\theta$ is defined as the angle between the polarization axes of the electric field and the molecular dipole vector axis.....	22
Figure 9. Example of alignment configurations for diatomic molecules placed in an external electric field. a) The left cartoon represents when the molecular axis is aligned perpendicular to the electric field. The middle and right cartoon are parallel with the electric field. The positive and negative signs denote if the molecular dipole is orientated with or opposite the electric field. b) The left, middle, and right cartoons signify perpendicular, isotropic, and parallel alignment. ....	23
Figure 10. Boltzmann distribution of the rotational energy levels, $J$ , of $N_2$ at atmospheric pressure .....	24
Figure 11. Adiabatic alignment dependence on the pulse duration [T. Seideman 1995].....	27
Figure 12. Adiabatic alignment of $I_2$ molecules. a) The expectation value of the $\langle \cos^2(\theta) \rangle$ of the $I_2$ molecules convoluted with the laser pulse. b) The expectation value of the total angular momentum squared. [H. Stapelfeldt 2003].....	29
Figure 13. Field-free alignment event from non-adiabatic alignment in $CO_2$ at 10 and 40 $TW\ cm^{-2}$ with no collisional effects, calculated by T. Seideman and S. Ramakrishna .....	30

Figure 14. Temporal evolution of the nonadiabatic revival events in N <sub>2</sub> . a) The experimental results from probe spectrum. b) Simulation of the nonadiabatic alignment in N <sub>2</sub> [F. Calegari 2008] .....	33
Figure 15. a) Cartoon of the experimental set-up of an OCS molecule oriented with its permanent dipole moment (bold red arrow) pointing in the direction of the static electric field. The left circularly polarized, LCP, probe pulse ionizes the molecule and imparts an upward momentum to the freed electron resulting in recording on the upper part of the detector. b) Two-dimensional momentum image of the electrons from a randomly oriented sample of OCS molecules ionized by the LCP pulse. c) The same as in b) but with a right circularly polarized, RCP, probe pulse. d) and e) are probed the same as b) and c), respectively, but the OCS molecules are oriented perpendicular to the image plane. [L. Holmegaard 2010 ] .....	35
Figure 16. <sup>15</sup> N <sub>2</sub> gas alignment signal. a) After the molecules were initially aligned, a second pulse illuminates them at the 3rd revival. The pulse coherently adds to the first one, enhancing the alignment. b) The second pulse arrives at an odd revival event, leading to an annihilation of the field-free alignment. [S. Fleischer 2008] .....	37
Figure 17. Schematic outline of the SpectraPhysics Spitfire laser .....	40
Figure 18. Gas chamber .....	41
Figure 19. Filament spectrum in 1 atm of CO <sub>2</sub> . The absence of CN dimers with the Violet band (0-0) transition bandhead at 388.5 nm, indicate that there is not N <sub>2</sub> in the chamber .....	42
Figure 20. Variable interferometer used for pump-probe method. Circles and dashes correspond to TE and TM polarizations, respectively .....	43
Figure 21. Experimental set-up for filamentation interaction with molecular alignment .....	44
Figure 22 Example image of the plasma emission from the filament interaction with CO <sub>2</sub> .....	45
Figure 23. Simulation of nonadiabatic molecular alignment of CO <sub>2</sub> by 19 TW cm <sup>-2</sup> 132 fs pulse, with a center wavelength at 810 nm, in 1 bar of pressure. Simulation by T. Seideman and S. Ramakrishna .....	48
Figure 24. The calculated alignment factor temporal dependence after excitation by a short strong laser pulse. The calculation is performed for 15N <sub>2</sub> at room temperature and atmospheric pressure. At the integer and half-integer multiples of the revival period, the molecular wave packet evolves between alignment (“cigar”) and anti-alignment (“disc”). [S. Fleischer 2008] ...	49

Figure 25. The degree of alignment dependence on different intensities of laser pulses with the same pulse duration .....	51
Figure 26. a) Full rotational period free field nonadiabatic alignment dynamics. b) and c) First revival event and fourth revival event, respectively .....	52
Figure 27. The nonadiabatic alignment pressure dependence for small deviations in pressure	54
Figure 28. Experimental results of the collapse position and the corresponding images of the filament plasma emission for times about the 3rd revival event. a) The filament in between the second and third alignment events. b) The filament polarization and molecular axis are orthogonal, thus the filament collapses later and the plasma length is decreased. c) The polarization and molecular axis are parallel, resulting in a closer collapse and longer plasma length. ....	55
Figure 29. a) The filament collapse position from the lens and b) filament length dependence on the time dependent molecular alignment. The grey shaded region and solid black line correspond to the standard deviation of the measurements taken and the average of the measurements respectively.....	57
Figure 30. Comparison of the simulated nonadiabatic alignment revival with decay effect included and the experimentally determined molecular alignment revival features.....	59
Figure 31. Comparison of the filament length and the collapse position molecular alignment dependence .....	61
Figure 32. Comparison of the theoretical population decay and experimental collapse position decay .....	63
Figure 33. The gray dotted curves are the experimental homodyne signals of the pump-probe measurement in CO <sup>2</sup> at 295 K. The red curve is the M-dependent model and the blue dash-dotted curve is the M-independent model. a) 2 bar with a peak intensity of 45 TW cm <sup>-2</sup> . The insert shows the features of the first revival. b) 20 bar with a peak intensity of 35 TW cm <sup>-2</sup> . [Th. Vieillard 2013] .....	65
Figure 34. Eriko later. Pulse duration measurement experimental set-up .....	73
Figure 35. Image from the Autocorrelation.....	74
Figure 36. Comparison of the autocorrelator and GRENOUILLE on the MTFL system .....	75

## LIST OF ACRONYMS

AR	Anti-Reflection
BBO	Beta Barium Borate
CCD	Charge-Coupled Device
CPA	Chirped Pulse Amplification
ECS	Energy Correction Sudden
FROG	Frequency-Resolved Optical Gating
FWHM	Full Width Half Max
GRENOUILLE	GRating-Eliminated No-nonsense Observation of Ultrafast Incident Laser Light E-fields
HHG	High Harmonic Generation
IR	Infrared
LIBS	Laser Induced Breakdown Spectroscopy
LIDAR	Light Radar
LPL	Laser Plasma Lab
LWFA	Laser Wakefield Plasma Acceleration
MTFL	Multi-Terawatt Femtosecond Laser
MOPA	Master Oscillator Power Amplifier
SHG	Second Harmonic Generation
TE	Transverse Electric
TM	Transverse Magnetic
UV	Ultraviolet

## 1 INTRODUCTION

The ability of lasers to generate high intensity pulses of light has led to many advances in non-linear optics and physics. The development of these high peak power lasers led to the discovery of femtosecond laser filamentation in air [A. Braun 1995]. Filamentation is a dynamic balance between non-linear Kerr self-focusing and plasma defocusing. Since the initial discovery of filamentation there have been extensive studies in several different applications. A few of the proposed studies include triggering and guiding of lightning, weather control (droplet and snowflake generation), high voltage spark gap discharge, generation of THz, UV to IR ultra broad continuum, generation of shorter pulses, waveguide writing, kilometer range LIDAR and LIBS as filamentation can propagate for more than a kilometer while maintaining high intensities [A. Couairon 2007].

During the past century there has been a significant study in the rotation and alignment of molecules. By studying the rotational properties of a gas through spectroscopy one can gain a plethora of information about the molecules' properties. For example, the alignment of these molecules can play a role in the dynamics of a chemical reaction. John Kerr (1875) showed how molecules can be used in the realm of optics. It was demonstrated that one could rotate the plane of polarization by passing the light through an optical medium subject to an applied electric field [R. Gray 1935]. Since his discovery there have been substantial advances in molecular alignment. By using short pulses of light one can induce static-field-like conditions of molecular alignment [B. Friedrich 1995]. Using ultrashort pulses, on the order of 100

femtosecond, one obtains complex highly temporal dependent alignment after the pulse has interacted with molecules [T. Seidman 1995].

The research detailed in this thesis expands on the topic of ultrashort pulse alignment and filament interaction with aligned molecules. Due to the properties required to generate a filament, it is affected by the spatial and temporal dynamics of aligned molecules. This has led to the proposition of using a filament as a probe of the temporal molecular alignment features.

This work is divided into 6 chapters. Chapters 2 and 3 will cover the introductory material of both filamentation (Chapter 2) and molecular alignment (Chapter 3). Chapter 2 will detail the physical mechanism and background information required to understand the filamentation process. Chapter 2 will also present various significant and related works in filamentation. Chapter 3 will cover the evolution of molecular alignment, from basic static fields to quantum mechanically rigorous ultrafast pulse interaction with molecules resulting in unique alignment capabilities. The experimental set-up used in this work is described in chapter 4. Our work in filament interaction with aligned molecules of CO<sub>2</sub> will be detailed in chapter 5. Chapter 6 will be the conclusion of this thesis.

## 2 FILAMENTATION

### 2.1 Introduction

The rise of high intensity lasers has led to many advances in non-linear optics and physics. The technique of chirped pulse amplification (CPA) allows for table top laser systems to have the capability of producing terawatts of peak power. CPA was first demonstrated by Mourou *et al.* in 1985. With the appearance of high peak power lasers, novel phenomena have been discovered and studied, such as ultra-short femtosecond laser filamentation. Femtosecond laser filamentation can be described as a dynamic balance between Kerr self-focusing and plasma defocusing to generate a nearly non-diffracting beam. Filamentation in air was first documented by Braun *et al.* in 1995. After its initial discovery, there was a boom of studies in several directions of interest simultaneously, as seen in the reference list. Large ranges of application have been proposed for laser filamentation. A few of such applications include guiding and triggering of lightning, weather control (droplet and snowflake generation), high voltage spark gap discharge, generation of THz, UV to IR ultra broad continuum, generation of shorter pulses, waveguide writing, kilometer range LIDAR and LIBS as filament can propagate for more than a kilometer while maintaining high intensities [A. Couairon 2007]. From this list of filamentation capabilities, this work will only detail the continuum generation, THz generation, microwave and electron guiding, high voltage gap discharge, and molecular alignment effects.



## 2.2 Ultrashort High Intensity Pulse Generation

### 2.2.1 Mode-locking

One method to produce an ultrashort pulse, on the order of a few femtoseconds, is through mode-locking. For mode-locking, one requires a gain medium with a broad spectral gain to allow short pulses and a cavity that permits many modes to exist. The interference of the different longitudinal modes, with a fixed phase relation, will generate an ultrashort pulse of light [A. E. Siegman 1986]. The duration of the pulse is directly related to the spectral bandwidth. For a Gaussian pulse, the pulse duration,  $\Delta\tau$ , and frequency bandwidth,  $\Delta\nu$ , are related through the time bandwidth product,  $\Delta\tau \Delta\nu = 0.441$  [J. Verdeyen 1995]. These pulses of light will appear as a pulse train [A. E. Siegman 1986]. There are two primary methods of mode-locking, active and passive mode-locking.

Active mode-locking requires a variable gain or loss element, such as an acousto- or electro-optical modulator [A. E. Siegman 1986]. Either device would modulate the resonator to allow for periodic amplitude modulation of a chosen frequency. When a mode in the cavity is amplified, it will generate frequency side bands at the mode frequency  $\pm$  the modulation frequency. These new frequencies will be amplified and generate their own sidebands respectively. This will continue until the entire gain frequency envelope of the gain material is amplified and phase locked. Another active method is synchronous pumping [A. E. Siegman 1986]. In this case, the laser is pumped with another ultrashort laser, typically another mode-locked laser. This technique requires that both laser cavities be identical.

Passive mode-locking uses a loss or gain element or/and geometry that is dependent on intensity, e.g. a saturable absorber [A. E. Siegman 1986]. A saturable absorber is placed inside the cavity, allowing for transmission of random high intensity spikes. The low intensity pulses

are not allowed to propagate in the cavity. As the random intensity spike continues in the cavity, it will be further amplified, increasing the intensity and contrast of the cavity. After a number of round trips, the laser produces a train of mode-locked pulses. Passive mode-locking allows for shorter pulse durations since they do not depend on the switching time of a modulator.

### *2.2.2 Chirped Pulse Amplification*

The basic principle of chirped pulse amplification, CPA, begins with an initial pulse that is generated with an oscillator able to produce short pulses with a broad spectrum [Mourou 1995]. By using a dispersive element (prism, grating, or grism) the pulse is temporally stretched by 3 to 5 orders of magnitude. This long pulse has a lower peak intensity, thus enabling the pulse to be amplified without damaging any of the optical components. After the stretcher, the pulse is then amplified by a factor of  $10^6$  and greater, depending on the amplifier system. Once the pulse is amplified, it must be temporally recompressed. This compression is usually achieved by using a series of gratings that match the inverse of the dispersion introduced by the stretcher. All lasers used in this dissertation work on this principle to generate pulses of ~100 to 50 fs with energy from 1 mJ up to a few hundred mJ.

### 2.3 Physics of Filamentation

The emergence of high peak power lasers led to the discovery of femtosecond laser filamentation. Filamentation is a dynamic balance between non-linear Kerr self-focusing and plasma defocusing. The resulting filament is filled with rich physics and applications.

### 2.3.1 Kerr Self-Focusing

When an intense electromagnetic field interacts with a medium, it experiences a spatial and temporal intensity-dependent refractive index contribution, where the pulse shape is imprinted on the medium. For a pulse that is Gaussian spatially and temporally, the refractive index profile would also be Gaussian. The refractive index is modified according to equation 1.

$$n(r, t) = n_0 + n_2 * I(r, t) \quad (1)$$

For most materials, the non-linear contribution to the refractive index  $n_2$ , is a positive contribution. Since  $n_2$  for air is about  $5.6 * 10^{-19} \text{ cm}^2/\text{W}$ , it is primarily only a concern for ultra-short high intensity pulses [S. L. Chin 2005]. However, for high intensity laser pulse, this addition to the index profile can lead to a beam that is able to overcome the spatial divergence due to diffraction; as it causes the beam to experience Kerr self-focusing. As the beam focuses, the on axis irradiance increases, leading to stronger self-focusing, further increasing the irradiance and so on. Once the ionization irradiance threshold is reached, it can lead to a breakdown of the material, leading to ionization, as shown in figure 1. To determine the propagation length of the beam for the initial collapse, one can use the well approximated the semi-empirical formula, equation 3 [J. H. Marburger 1975].  $L_c$  and  $L_{DF}$  are the collapse length and the Rayleigh length of the beam, respectively.

$$L_c = \frac{0.367L_{DF}}{\sqrt{\left[\left(\frac{P_{in}}{P_{cr}}\right)^{\frac{1}{2}} - 0.852\right]^2 - 0.0219}} \quad (2)$$

### 2.3.2 Plasma Defocusing

Plasma contributes a negative focusing effect, which will diverge the beam. The index modification due to plasma follows equation 4 based off the Drude model [A. Couairon 2007].

$$n \simeq n_0 - \frac{\rho(r,t)e^2}{\omega_0^2 m \varepsilon_0} \quad (3)$$

$n$  is the plasma index of refraction,  $\rho$  is the electron density,  $e$  is the charge and  $m$  is the mass of an electron,  $\varepsilon_0$  is the permittivity in vacuum, and  $\omega_0$  is the center angular frequency of the laser. The primary ionization processes in the filamentation regime are multiphoton and tunneling ionization.

Multiphoton ionization can be described as the process of a material simultaneously absorbing multiple sub-ionization energy photons to free an electron. Oxygen, which is the easiest component of air to ionize, requires approximately 13.6 eV [C. Cornaggia 2000]. For a laser at 800 nm, this would require about 8 photons, 800 nm  $\approx$  1.55 eV. The self-focusing beam will ionize oxygen before nitrogen due to its lower ionization potential energy, 13.6 eV verses 14.5 eV. The rate of ionization scales as  $I^K$ , where  $K$  is the number of photons required to induce ionization. Tunneling ionization distorts the atomic energy levels of the material increasing the probability for an electron to tunnel through the material. Laser filamentation is on the edge of the intensity of the two regimes, multi-photon and tunnel ionization, and one or the other should be considered as the predominant phenomena as function of the experimental condition.

The reported values of filamentation plasma density experimentally measured and theoretically calculated from different groups vary greatly from  $10^{12}$  to  $10^{18}$  cm<sup>-3</sup>, depending on the filamentation conditions, such as the use of a lens to accelerate the apparition of filamentation [B. La Fontaine 1999, H. Schillinger 1999, S. Tzortzakis 2000, F. Théberge 2006, Y. H. Chen 2010]. There are several factors that contribute to this wide range of values including measurement techniques, single vs. multiple filaments, focusing conditions, gases used, and

pulse duration. The generation of plasma leads to the defocusing of the intense laser beam, then the dynamics competition between Kerr focusing and plasma defocusing clamps the maximum intensity a filament can contain, see figure 1 [S.L. Chin 2002]. If the power of the beam is above the critical power,  $P_{cr}$ , the nonlinear self-focusing is able to overcome the divergence [J. H. Marburger 1975].

$$P_{cr} = \frac{3.72\lambda_0^2}{8\pi n_0 n_2} \quad (4)$$

$\lambda_0$  is defined as the center wavelength of the spectrum of the pulse of light. This critical power is valid for a Townes beam profile. For a standard Gaussian beam, the constant of 3.72 would be replaced by 3.77. A linearly polarized pulse with a duration of 100 fs centered at 800 nm leads to a clamping intensity approximately equal to the critical power of about  $1.8 * 10^{13} \text{ W cm}^{-2}$ .

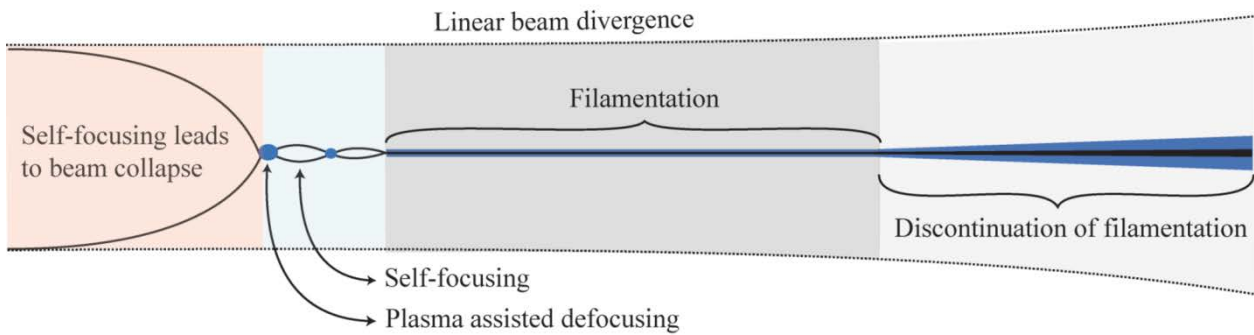


Figure 1 Filamentation propagation dynamics

### 2.3.3 Multiple Filaments

As explained in the previous section, a high intensity pulse with the critical power for filamentation,  $P_{cr}$ , undergoes collapse due to Kerr effect and then starts the process of

filamentation by generating plasma that adds the defocusing effect to the propagation dynamics. However, if the peak power of the laser beam is more than twice the critical power  $P_{cr}$ , the beam will split into multiple filaments rather than one filament due to intensity clamping limiting the amount of energy that can be injected into one plasma channel. The beam will, in this case, form multiple plasma channels that usually spring from the hot spots, regions of high intensity in the beam profile. As the appearance of those high intensity regions are usually not manufactured, the process emerges from the noise of the beam profile or turbulence during the linear propagation, rendering the position of the multi-filament inside the beam profile unstable from shot to shot. Solutions to control the position of those multi-filaments inside the beam profile has been developed inside the LPL team and other researchers [D. Walter 2007, H. Takahashi 2007, T. Grow 2006, E. Matsubara 2007]; by adding a predetermined phase to the beam, multi-filaments structured were engineered [N. Barbieri 2011].

Even for a perfect linearly polarized Gaussian beam profile, multiple filaments will still form if the beam has enough energy [G. Fibich 2003]. It has been shown that circular polarization with a perfectly circularly symmetric profile theoretically will suppress multiple filaments, allowing for a high energy filament [G. Fibich 2003, N. A. Panov 2011]. Perfect beam profiles do not exist realistically but it has been shown experimentally how circular polarization can reduce multiple filaments by lowering the effect of  $n_2$ , and improve pointing stability [A. Trisorio 2007].

#### 2.3.4 Continuum Generation with Filamentation

Filamentation is a complex highly nonlinear system that allows for several frequency generation processes to occur. Filamentation strongly spectrally broadens the pulse through self-phase modulation, ionization, and self-steepening [A. Couairon 2007]. Self-phase modulation stems from the temporal Kerr effect of self-focusing. In the section on the Kerr effect, only the spatially dependent focusing effect was highlighted, however, the index of refraction profile is dependent on both the spatial and temporal profile of a pulse. In a normal dispersion Kerr medium, the front of the pulse will generate red frequencies whereas the trailing edge will produce blue frequencies. For a transform limited pulse, the spectrum will become chirped, broadening the pulse. If the spectrum is down chirped, the spectral phase modulation can cause spectral compression depending on the dispersion regime the material is in (normal or anomalous).

In addition to the process of self-phase modulation, the spectrum of the filamenting beam will also be influenced by the multiphoton ionization, which has been shown to spectrally blue shift the spectrum of a pulse [M. Kolesik 2003]. Another spectral change of the filamenting beam is due to self-steepening; which is the result of the effect from a Gaussian pulse peak slowing with respect to the group velocity, allowing the trailing portion to catch up. This causes a steep edge in the trail of the pulse, leading to the trailing edge to experience a stronger Kerr effect, and thus generating more blue frequencies than red [Rothenbeg 1992].

Filaments have been shown to generate ultra-broad spectra that can expand from 0.2 to 8  $\mu\text{m}$  in fluoride glass [Meisong Liao 2013]. There have been several efforts to extend the supercontinuum generation to higher frequencies, such as using a 40 fs pulse and third harmonic generation for 230 nm emission [N. Aközbeğ 2003]. Few cycle pulses,  $\sim 6$  fs, are able

to extend the spectrum to 210 nm [N. Aközbek 2006]. Other novel techniques for supercontinuum manipulation include molecular alignment assistance [H. Zeng 2009, H. Zeng 2010], anomalous dispersion for extreme blue shifted peaks [M. Durand 2013], using 100 TW pulses for 1 Joule of white-light continuum [J.P. Wolf 2011], and even using human saliva for continuum suppression [S. Chidangil 2007].

The supercontinuum generation, is emitted as a conical emission. This is one of the most recognized signatures of filamentation. It consists of a white center where the supercontinuum is located with an inverted rainbow-like distribution, the reds being more centralized and the blues located further on the outer rings, as seen in figure 2. There have been several different theories to explain conical emission including Cerenkov radiation [E. T. J. Nibbering 1996], X-waves [P. Maioli 2009, P. Di Trapani 2007], and four wave mixing [G. G. Luther 1994, T. Fuji 2012].

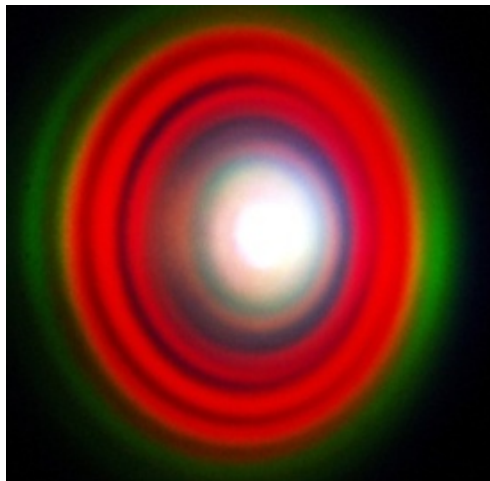


Figure 2 Conical emission from filament propagation in the normal dispersion regime [M. Durand 2011]



### 2.3.5 THz Generation

It has been observed that the plasma created from filaments can generate electromagnetic radiation in the THz frequencies. THz is a useful frequency range for spectroscopy, fundamental physics, and imaging. Many molecules have rotational and vibrational transitions in this frequency range. Since THz has low photon energy, it can penetrate many materials and not damage/alter biological tissues. Propagation of THz radiation over long distances in air is difficult due to the water absorption in the atmosphere having strong absorption in the THz band. Filaments are a potential solution to this problem since they are able to project energy well past the diffraction limit [G. Méchain 2005]. The plasma from the filament can then be generated near a target, in turn producing the desired THz to probe the chosen target.

S. Tzortzakis et al. (2000) were first to show that filaments generate THz in the transverse direction of the filament. Cheng et al. (2001) proposed that the charge separation due to the radiation pressure is what leads to radial THz generation. Then a more intense forward emission was discovered and was explained in terms of Cherenkov radiation [D'Amico 2007]. The proposed Cherenkov radiation was generated by the ionization-front reaching superluminal velocities [Sprangle 2004]. If a plasma string was infinite in length, it would be unable to generate THz. Thus the inherent finite length of the filament plasma is required and determines the emission angle [D'Amico 2008]. A more detailed explanation of single color filament THz generation can be found in D'Amico et al. (2008).

In order to enhance the generation of THz from a filament, a local electric field to accelerate the electrons can be created by using a "two-color" filament. In order to create a two-color filament, one must pass the beam through a nonlinear frequency doubling crystal

such as beta barium borate (BBO). The beam will then contain both the fundamental frequency and the second harmonic frequency pulses with different polarizations. In order to compensate for the polarization difference and dispersion, one must place wedges and a dual wavelength wave plate in the beam path, as shown in figure 3. The two main models for two-color filaments are four-wave mixing and the photo-current model. The four-wave mixing is based on third order nonlinearity, a thorough explanation can be found in these references [D. J. Cook 2000, M. Kress 2004, T. Bartel 2005, X. Xie 2006]. The photo-current model points to the free electron drift current between the fundamental and the second harmonic frequencies for THz generation [K. Y. Kim 2008, N. Karpowicz 2009]. T. J. Wang et al. (2010) showed that the THz generation was not changed by applying an external DC electric field across the filament. That experiment may indicate that the four-wave mixing is the dominate mechanism for THz generation, but more experiments are required to separate the contributions from each model [T. J. Wang 2010].

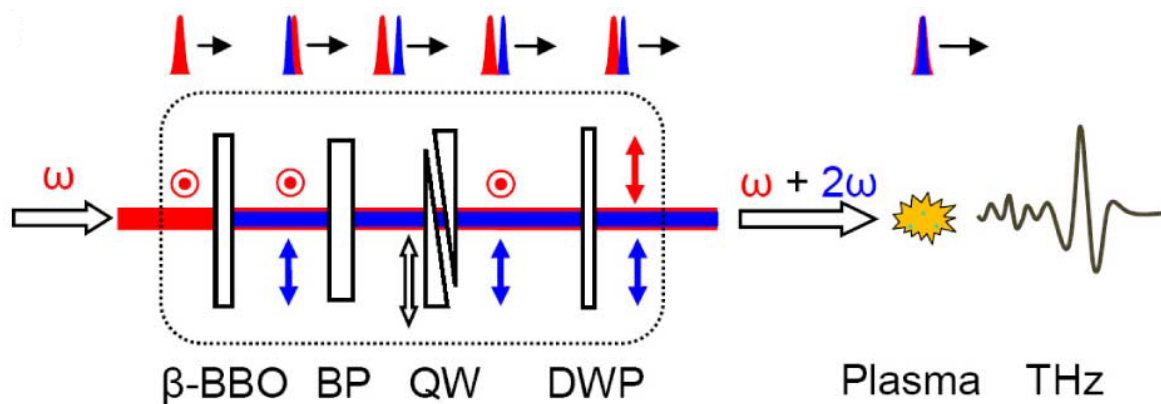


Figure 3. Two-color filament for THz generation setup [J. Dai 2010]

### 2.3.6 Guiding with Filamentation

Filamentation has unique properties that gives it advantages for guiding; e.g. overcoming the Rayleigh diffraction limit and cylindrically symmetric plasma columns, such as electron guiding, microwave guiding, and controlled electrical discharge. One specific example of electron guiding involves laser wake-field plasma acceleration. LWFA, laser wake-field plasma acceleration, uses ultra-high intense electric fields and generates high energy electrons whose energy can be limited by electron dispersion and diffraction. An in depth review of laser induced electron acceleration can be found in [E. Esarey 2009]. C. G. R. Geddes et al. (2009) were able to use filamentation plasma channels to overcome the Rayleigh range by a factor of ten. They created a plasma column with a 60 fs, 15 mJ pulse of which was heated via inverse Bremsstrahlung with a 250 ps, 150 mJ pulse. A 55 fs, 500 mJ was then focused at the edge of the plasma with an intensity of  $1.1 * 10^{19} \text{ W cm}^{-2}$ . They were able to produce electrons with MeV of energy that were only tightly confined with narrow energy deviation while the filamenting plasma column was present.

Microwave guiding with filaments can be achieved by several techniques and filament geometries. For single filaments, the microwave radiation propagates as a surface wave down the column of plasma [Y. Ren 2013]. Theoretically, the multiple filaments could be arranged in a guiding structure similar to a fiber. The microwaves would be confined to an effective medium structure that allows for reflection off the plasma wall permitting propagation over long distances [Z. Kudyshev 2013]. The microwave guiding efficiency is determined by the number of filaments and their geometric configuration. By using a hollow core fiber geometry, microwave radiation from millimeter to centimeter can be guided [M. Alshershby 2012]. In addition to the microwaves ability to be guided, the microwaves could be used as a diagnostic

tool for the filaments themselves. The microwaves, for example, could be used to determine the effective plasma density.

Filamentation is a possible solution to man's desire to control lightning. Experiments have shown that by propagating a filament with a high voltage electrical discharge, one can direct the electric discharge to a desired path, e.g. figure 4 [P. Rambo 2001, M. Rodriguez 2002, A. A. Ionin 2012, B. Forestier 2012, M. Henriksson 2012, S. B. Leonov 2012]. Triggering electrical discharges has been performed since the 1970's using nanosecond pulses, but was limited due to the discontinuous plasma columns and plasma's inherent absorption [S. Uchida 1999]. Soon after the discovery of filamentation, filaments were used for guiding high voltages to create short circuits [X. M. Zhao 1995]. The guiding capabilities have been shown to last for periods up to a few microseconds after a filament [B. La Fontaine 2000]. Through the ionization of the air, the filament decreases the distance of a gap for the high voltage discharge by 50% in comparison to spontaneous discharge [H. Pepin 2001]. Though both single filaments and multiple filaments will induce electrical discharges, it was shown that the minimum threshold for breakdown did not increase with the number of filaments, but the discharge path length was shown to increase [K. Guo 2012].

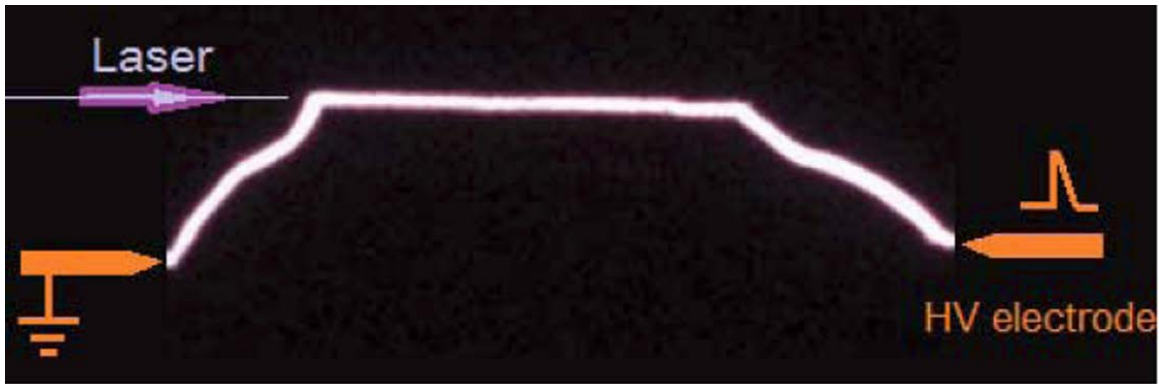


Figure 4. Raw image by S. B. Leonov et al. (2012) of filamentation induced high voltage electrical discharge

In the following section, the role of molecular orientation will be detailed in the ways that the filamentation process can be affected. Controlling molecular orientation can have many beneficial effects, including, but not limited to: increasing plasma density and length [S. Varma 2012], affecting THz generation [M. Durand 2010], frequency shifting [J. Wu 2009], and pulse duration dependent non-linear index of refraction [J.-F. Ripoche 1997].

### 3 MOLECULAR ALIGNMENT

#### 3.1 Introduction

Electromagnetic radiation can interact with the internal degrees of freedom of a molecule, such as the electronic, vibrational, and rotational states. As an example, figure 5 shows the different energy levels of a diatomic molecule. The resonant rotational wavelengths are much longer than the vibrational or electronic resonances. Rotational wavelength resonances are between  $300\ \mu\text{m}$  to  $30\ \text{cm}$  ( $4.1\ \mu\text{eV}$  –  $4.1\ \text{meV}$ ,  $1\ \text{GHz}$  to  $1\ \text{THz}$ ) in comparison to  $4 - 50\ \mu\text{m}$  ( $310\ \text{meV}$  –  $24.8\ \text{meV}$ ,  $2500 - 200\ \text{cm}^{-1}$ ) for vibrational and  $< 1\ \mu\text{m}$  for electronic resonances.

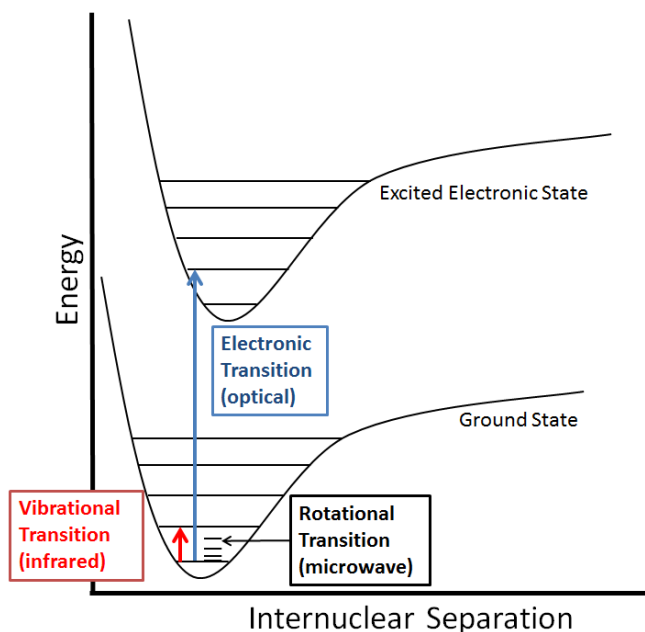


Figure 5. Typical energy levels of a diatomic molecule.

The classical energy of rotation is defined in equation 5.  $I$  is the moment of inertia [ $\text{kg m}^2$ ],  $\omega$  is the angular frequency [ $\text{s}^{-1}$ ], and  $L$  is the angular momentum [ $\text{J s}$ ].

$$E_{rot} = \frac{1}{2} I \omega^2 = \frac{L^2}{2I} \quad (5)$$

This approach of rotation is only valid for classic macroscopic objects. Therefore, when considering molecules, one must switch to the quantum mechanical treatment. From the Schrödinger equation, only quantized rotational energy states are allowed. These eigenmodes are what determine the possible energy configurations of a system, equation 6 [D. Griffith 1995].

$$E_{rot}^J = \frac{J(J+1)\hbar^2}{2I} = J(J+1)\hbar\omega_{rot} \quad (6)$$

Here  $E_{rot}^J$  is the rotational energy with respect to  $J$ .  $J$  is the total angular momentum quantum number,  $\hbar$  is the reduced Planck's constant, and  $\omega_{rot}$  is equal to  $\hbar/2I$ . Each eigenmode is associated to an eigenfunction, i.e. rotational wavepacket. Figure 6 shows the rotational spectrum of CO at 300 K [S. Mackenzie 2012]. The transmission lines are in the microwave region, between 1 cm and 100  $\mu\text{m}$ . The lines are spaced by  $3.86 \text{ cm}^{-1}$  corresponding to twice the rotational constant of CO,  $1.93 \text{ cm}^{-1}$  in the ground state.

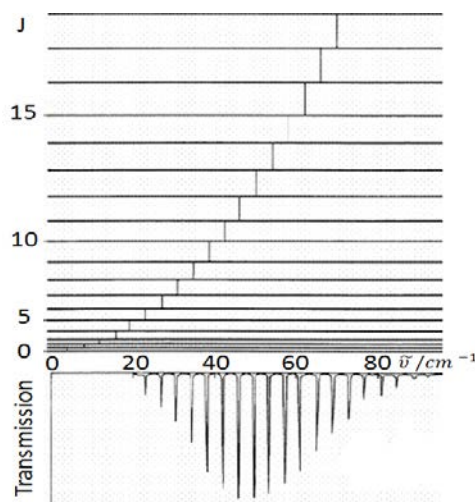


Figure 6. Rotational spectrum of CO at 300 K [S. Mackenzie 2012]

The rotational period of a molecule depends on its reduced mass and equilibrium nuclear distance. For a non-symmetric molecule there are three axes of rotation. Each of these axes has their own constant of rotation, A, B, C. The number of axes for linear molecules reduces to one degenerate axis of rotation, B. One can calculate the rotational constant,  $B_0$ , for a linear molecule using equation 7 in the approximation of the rigid rotor. Once the  $B_0$  is known one simply applies it to equation 8 to obtain the rotational period of the molecule. For example  $N_2$  or  $O_2$  rotational constants are 2.01 and 1.45  $\text{cm}^{-1}$ , and thus have rotational periods of 8.3 and 11.6 ps respectively [N. Xu 2008].

$$B_0 = \frac{\hbar}{4cMR_e^2} \quad (7)$$

$$\tau_{rot} = \frac{1}{2cB_0} \quad (8)$$

For the equations above, the constants  $B_0$  [ $\text{cm}^{-1}$ ],  $\tau_{rot}$  [s],  $\hbar$  [Js],  $c$  [cm/s],  $M$  [kg], and  $R_e$  [cm] represent the rotational constant, rotational period, reduced Planck's constant, speed of light, the molecule's reduced mass, and the equilibrium nuclear distance, respectively.

If one wants to align molecules, there are several techniques that have been used. The relevant time scales for molecular interactions are shown in figure 7. Molecules that have an intrinsic or induced dipole moment can align in an electric field. The dipole moment is proportional to the electric field and the polarizability. The polarizability,  $\alpha$ , is a second rank tensor, as such it allows for anisotropy in the different axes. This polarizability permits a molecule to have different induced dipole moments in the molecule's axes. In the case of a linear molecule the polarizability difference,  $\Delta\alpha$ , is the difference between the parallel axis polarizability and the perpendicular axis polarizability with respect the molecules orientation



with the electric field. Molecules without an intrinsic dipole can still be aligned by inducing a dipole. The induced dipole results from the polarizability of the molecule interaction with the electric field. The electric field will rearrange the electron distribution to induce a dipole. One can use the torque exerted on a molecule's dipole from the electric field to rotate the molecule. For example, by applying an electric field to liquid crystals the molecules rotate to align their dipoles with the direction of the electric field. This work will focus on the alignment of gases, which have more rotational freedom than liquids or solids.

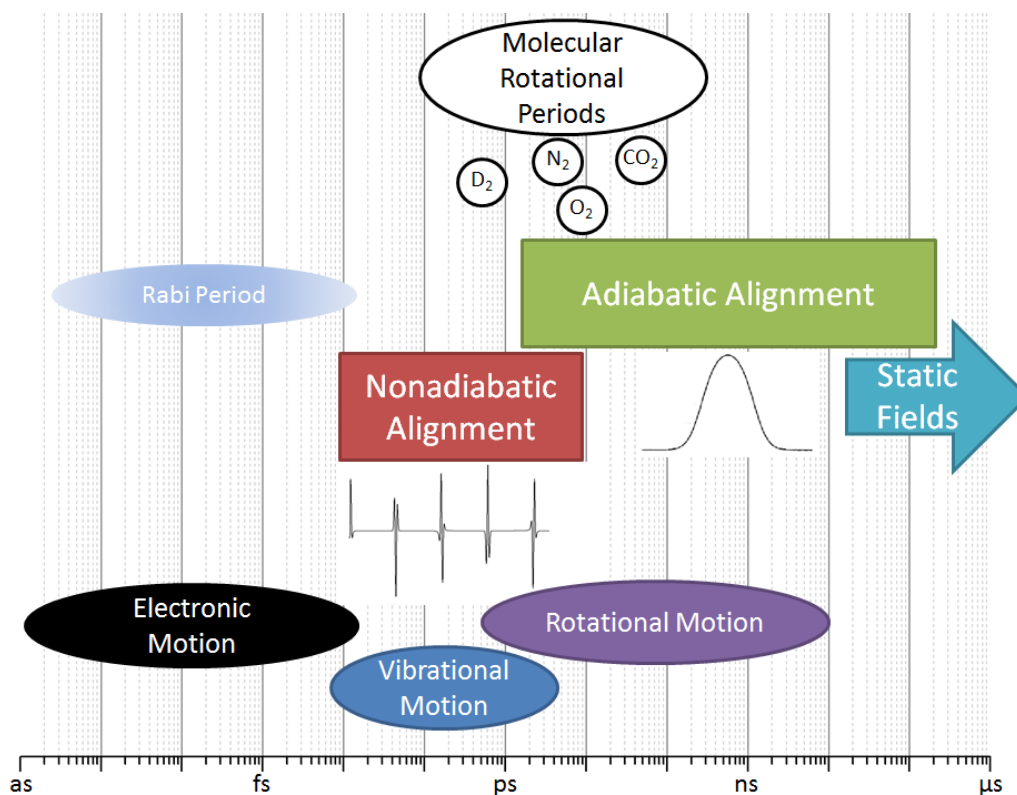


Figure 7. Relevant time scales for molecules

But there is a limit to the strength of static fields that can be used to align molecules. Air molecules will experience dielectric break down and ionize with fields greater than dielectric

strength of air, approximately 3 kV/mm [J. R. Dwyer 2003]. There is also a technical limit for producing the required field strengths. Another method of alignment that is capable of producing strong electric fields involves using an electromagnetic pulse. One can study the interaction of the molecules and an electric field in the Hamiltonian formalism. By using the rigid rotor eigenstates, the field-free and field interaction Hamiltonians,  $H_0$  and  $H_{int}$ , can be written as

$$H_0 = \sum_{JM} \varepsilon_J |JM\rangle \langle JM| \quad (9)$$

$$H_{int} = -\frac{1}{4} E(t)^2 \sum_{JJ'M} \left( \begin{array}{c} \Delta\alpha \langle JM | \cos^2(\theta) | J'M \rangle |JM\rangle \langle J'M| \\ + \alpha_+ |JM\rangle \langle JM| \end{array} \right) \quad (10)$$

with  $\varepsilon_J = B_0 J(J+1)$  the energy eigenvalues in the rigid rotor approximation,  $E(t)$  the electric field pulse envelope,  $\Delta\alpha = \alpha_{//} - \alpha_+$  the polarizability anisotropy (difference in polarizability of the different axes),  $J$  is the total angular momentum quantum number,  $M$  the quantum number of the projection of angular rotation states on  $J$ , and  $\langle \cos^2\theta \rangle$  represents the expectation value for the degree of alignment of the molecules. The angle  $\theta$  used is defined as the angle between the molecular dipole axis and electric field polarization, figure 8.

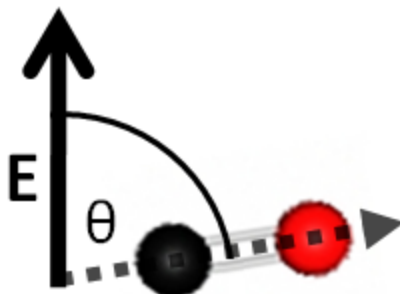


Figure 8. The angle  $\theta$  is defined as the angle between the polarization axes of the electric field and the molecular dipole vector axis

The orientation of molecules is dependent on the relationship of each molecule having the same atom in the same angular position with respect to the electric field and other atoms in the molecule. The alignment is simply the amount the molecule aligned with the electric field polarization. See figure 9 for a visual representation of orientation versus alignment. The  $\langle \cos\theta \rangle$  value corresponds to the expectation value for the degree of orientation of the molecules. A  $\langle \cos\theta \rangle$  value equal to zero represents the molecules lying perpendicular to the electric field.  $\langle \cos\theta \rangle = \{1, -1\}$  is when the molecular dipole axis is in the same plane as the polarization of the E-field. The dot product of the dipole and electric field determines the sign of  $\langle \cos\theta \rangle$ . An isotropic distribution of the molecular axes gives  $\langle \cos^2\theta \rangle$  a value of  $1/3$ .  $\langle \cos^2\theta \rangle$  values of 0 and 1 correspond to perpendicular and parallel alignments of the molecular and polarization axes, respectively.

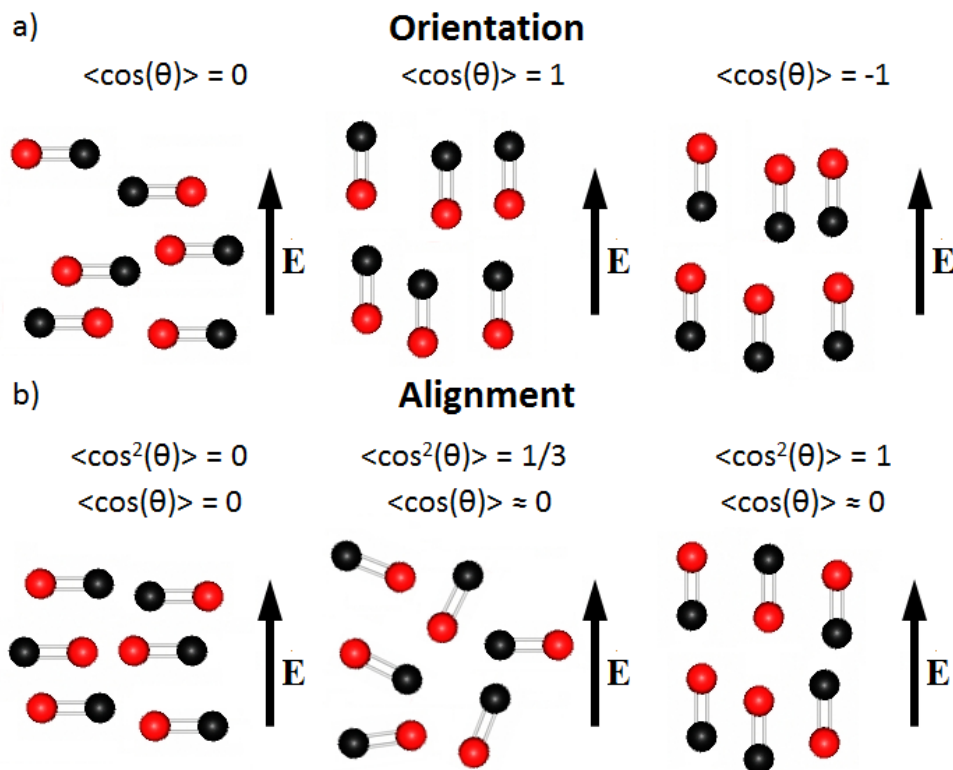


Figure 9. Example of alignment configurations for diatomic molecules placed in an external electric field. a) The left cartoon represents when the molecular axis is aligned perpendicular to the electric field. The middle and right cartoon are parallel with the electric field. The positive and negative signs denote if the molecular dipole is orientated with or opposite the electric field. b) The left, middle, and right cartoons signify perpendicular, isotropic, and parallel alignment.

Collisions and temperature play a significant role in the alignment of molecules. After the molecules have interacted with the electric field and are in a field free condition, the inelastic collisions lead the molecules to lose their alignment and return to equilibrium [S. Ramakrishna 2006]. By comparison, the molecules in liquids can too be rotated by electric fields. The alignment is limited by the many collisions and the coupling to the surrounding molecules. Therefore, the spectral features of the liquid will experience high dampening and broadening due to these collisions. This can be explained through the Debye model of liquids

[P. Debye 1929]. On the contrary, gases do not have many interactions and are weakly coupled, thus have longer periods of alignment before returning to equilibrium conditions.

The other factor that plays a significant role in the alignment of molecules is the temperature. The temperature of the system will populate the rotational energy levels in a Boltzmann distribution [Nan Zu 2008, T. Seideman 1995], figure 10. Molecules with highly populated rotational energy levels will be more difficult to align as the electric field must be able to overcome their angular momentum. High temperature gases would then require stronger electric fields. In order to have more uniform alignment, the molecules must have low rotational temperatures ( $< 10$  K). One method to control the rotational temperature is through supersonic expansion [J. B. Anderson 1966, H. Haberland 1985]. As the molecules expand into a vacuum they experience collisions that limit the rotational angular momentum to only be aligned favorably orthogonally to the direction of flight [V. Aquilanti 1999].

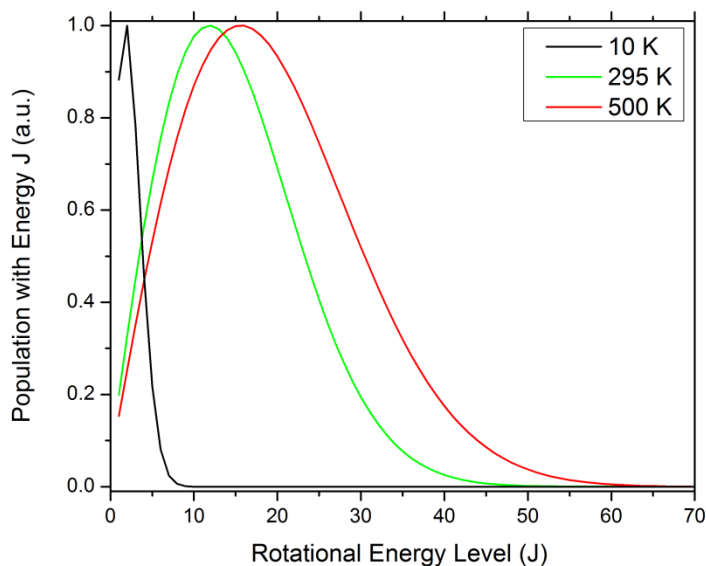


Figure 10. Normalized Boltzmann distribution of the rotational energy levels,  $J$ , of  $N_2$  at atmospheric pressure

### 3.2 Static Field Alignment

Static electric fields allow for the manipulation of both the alignment and the orientation of molecules. The hexapole focusing technique aligns symmetric top molecules through the first order Stark effect [M. Härtelt 2008, D. Parker 1989]. Hexapole focusing is based upon the principle of rotational selection. A symmetric polar molecule placed in an electric field,  $\mathbf{E}$ , and can be described by its  $|JKM\rangle$  states.  $J$  is the quantum number of the total angular momentum without nuclear spin,  $K$  is the projection of the rotational momentum on  $J$ , and  $M$  is the projection on the space-fixed axis of  $J$ . The average molecular alignment about the polarization of  $\mathbf{E}$  is shown in equation 11 [B. Friedrich 1991, D. Parker 1989].

$$\langle \cos\theta_{\mu,E} \rangle = KM/J(J + 1) \quad (11)$$

$\theta$  is the angle between the electric field  $\mathbf{E}$  and the dipole moment  $\mu$ . If the field  $\mathbf{E}$  has a radial component, the force on the molecule is

$$\mathbf{F}_r = -\frac{\partial W}{\partial r} = \mu_{eff} \left( \frac{\partial E}{\partial r} \right) \approx \mu \langle \cos\theta \rangle \left( \frac{\partial E}{\partial r} \right) \quad (12)$$

$W$  is the work [J],  $\mu_{eff}$  is the effective dipole =  $-(\partial W/\partial |\mathbf{E}|)$  and for molecules that are symmetric and polar it is equal to  $\mu\langle\cos\theta\rangle$ . All of the molecules with the same  $J$ ,  $K$ , and  $M$  states will have identically the same rotational energy and thus have the same degree of alignment. The molecules in an octahedral field were able to have the ground state density confined to the polarization axis even with the enhanced alignment from an intense laser pulse [T. Kiljunen 2005]. This allows for preparing suitably aligned precursor states to efficiently control subsequent direction-dependent reaction mechanisms [T. Kiljunen 2005]. The “straight forward” technique uses a strong static field. This technique can only be applied to polar molecules. When the molecules are placed in a DC electric field, the field strength must be able

to overcome the rotational energy to align the molecules [B. Friedrich 1991, M. Wu 1994]. The molecules that are better suited for this method are supersonically cooled and possess a significant dipole moment. Both of the static field techniques allow not only alignment but also orientation of molecules with respect to each other [B. Friedrich 1991, D. Parker 1989]. An interesting application of the DC electric field alignment was their use to grow aligned multi-wall carbon nanotube networks in epoxy composites [C.A. Martin 2005].

### 3.3 Adiabatic Alignment

The success of DC alignment suggested that molecular alignment can be induced using an alternating electromagnetic field. One of the primary advantages of using a laser pulse stems from the fact that the field strength required to exert an adequate torque on a molecule, that is either polar or nonpolar, can be easily achieved. In the limit of adiabatic alignment, the ability to align molecules with lasers was first shown by B. Friedrich et al. (1995). Adiabatic alignment corresponds to the case, where the pulse duration of the laser is larger than the duration of the rotational period of the molecule. Due to the strong field associated with the laser pulses, the molecule can obtain an induced dipole moment. This allowed nonpolar molecules without a permanent dipole to be aligned. Figure 11 is an example of enhanced alignment only during the duration of the pulse. They can only be aligned and not orientated due to their lack of a permanent dipole [H. Sakai 1999].

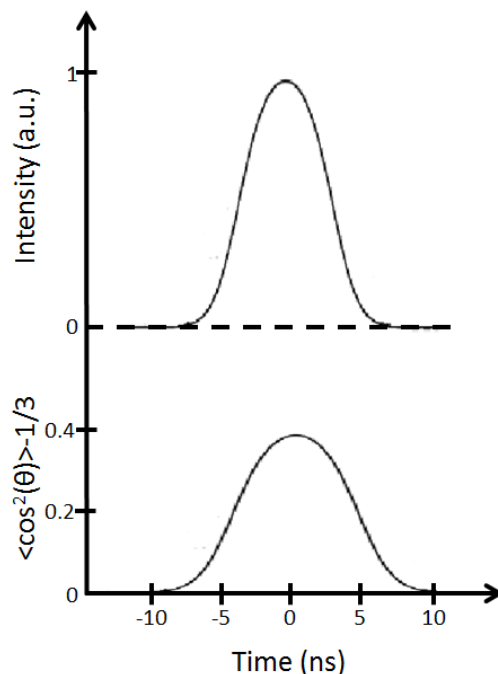


Figure 11. Adiabatic alignment dependence on the pulse duration [T. Seideman 1995]

The simplest method of alignment is the use of a CW electromagnetic signal from a laser. The eigenstates of Hamiltonian will evolve according to the Hamiltonian of a molecule in a field of constant irradiance. In this case one does not have to consider the dissipative dynamic effects. As a result of the pulse duration being larger than the rotational period the Hamiltonian will only evolve within the temporal duration of the pulse. After the pulse has passed, “turned off”, the Hamiltonian will return to the standard isotropic field-free state. Due to the effects only being present when the pulse is directly interacting with the molecule, the problem can be reduced to the intensively studied problem of inducing pendular states from a continuous field [T. Seideman 1995]. For adiabatic alignment, the molecules’ eigenstates, the pendular states, consist of a superposition of the field-free rotational states [B. Friedrich 1995]. The eigenstates



are termed pendular states since the molecules move about the polarization axis rather than being able to rotate freely, similar to that of a pendulum.

In order to illustrate adiabatic alignment we will consider the alignment of  $I_2$  molecules. H. Stapelfeldt et al. (2003) used the exact solutions of the time-dependent Schrödinger equation for their calculations. The laser pulse used had a Gaussian temporal duration of 3.5 ns and a peak intensity of  $1 \text{ TW cm}^2$ . Heavy molecules, such as  $I_2$ , are able to obtain strong alignment, even if they are nonpolar, due to their capability of having a strong dipole moment interaction. Lighter molecules can have an induced dipole by stronger fields, thus can also be aligned. When the molecules interact with the field they begin to rotate about the polarization axis. In figure 12 a, one can see how in the presence of the field the system obtains alignment up to  $\cos^2\langle\theta\rangle \geq 0.8$ . After the molecules are no longer in the field of the pulse they return to their isotropic distribution of  $\langle\cos^2(\theta)\rangle = 1/3$ .

As mentioned previously, the temperature plays a significant role for alignment of molecules. The higher the temperature, the higher rotational energy levels of the molecules will be additionally populated. The initial Boltzmann distribution of the rotational levels provides an equal amount of populated rotational levels up to the highest thermally populated rotational level [S. Ramakrishna 2006]. Figure 12 a shows the experimentally determined  $\cos^2\langle\theta\rangle$  value of the molecules with respect to time and temperature [H. Stapelfeldt 2003]. It is ideal to have all of the molecules in a low temperature, near 0 K, as this forces them to have nearly equivalent rotational energy states, see figure 12 b.

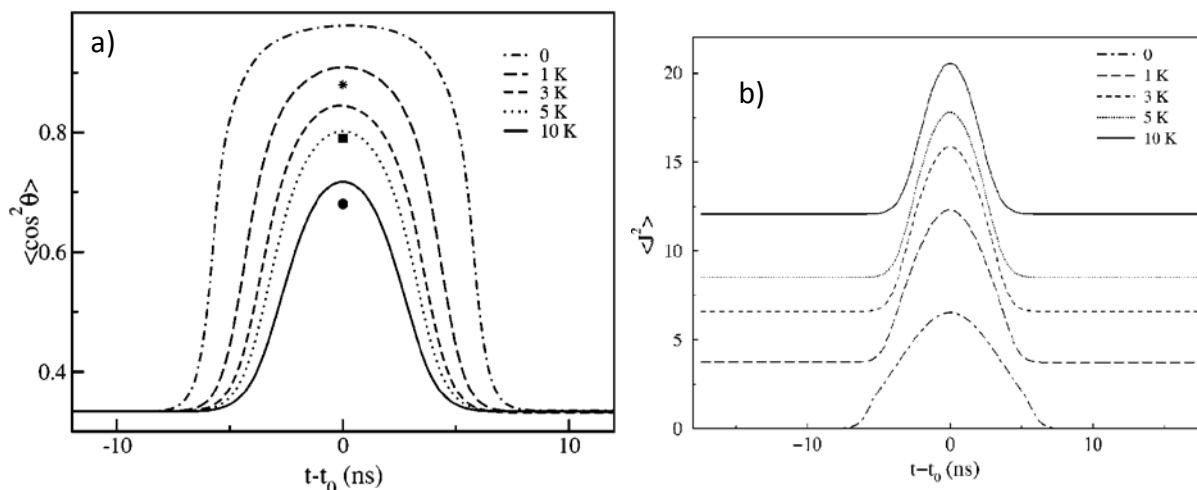


Figure 12. Adiabatic alignment of  $I_2$  molecules. a) The expectation value of the  $\langle \cos^2(\theta) \rangle$  of the  $I_2$  molecules convoluted with the laser pulse. b) The expectation value of the total angular momentum squared. [H. Stapelfeldt 2003]

The ability to directly control the molecules' alignment exclusively during the field interaction is both the advantage and disadvantage of adiabatic alignment. Studies of certain chemical reactions, that are sensitive to the alignment of the molecules, need to be free of an external field. Otherwise these strong fields would then change the chemistry of the interactions. The solution to having alignment without an external field, also known as field-free alignment, comes from aligning molecules using an ultrashort pulse. The pulse duration of the field must be much shorter than the rotational period of the molecules. This technique is known as non-adiabatic, or delta kick, alignment.

### 3.4 Non-adiabatic Alignment

When an ultrafast laser pulse, with respect to the rotational period of the molecule, with linear polarization interacts with molecules, it will "kick" them, spinning them about the

axis of the polarization. This will populate the higher J energy levels of the molecules. The excited J energy states will then decay. The resulting rotational wave packets will interfere. As the quantum rotational wave packets interfere, the molecules will experience periodic field-free revival alignment events as shown in figure 13. In this delta kick method, the temporal pulse duration of the electromagnetic field must be much shorter than the rotational period of the molecules but still longer than the Rabi period. The Rabi period is the probability of population time for an atomic transition near the molecule's electronic resonance.

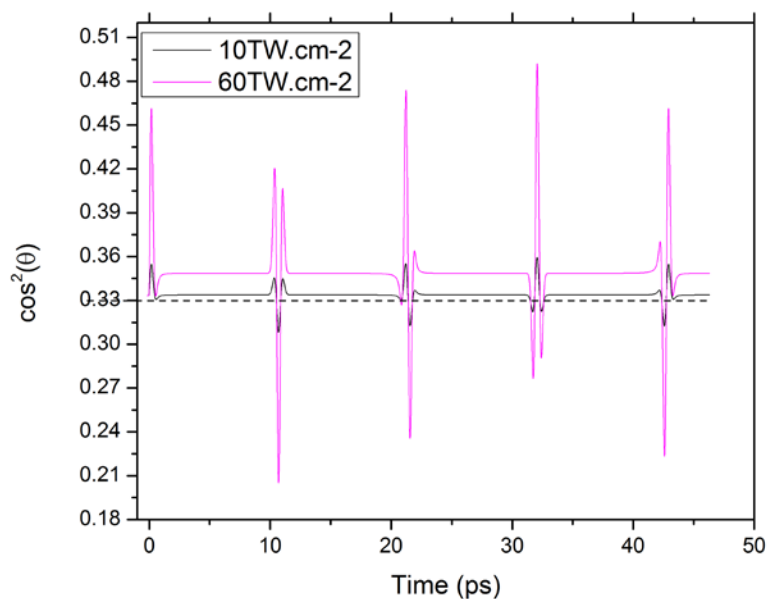


Figure 13. Field-free alignment event from non-adiabatic alignment in  $\text{CO}_2$  at 10 and 40  $\text{TW cm}^{-2}$  with no collisional effects, calculated by T. Seideman and S. Ramakrishna

The theory behind non-adiabatic alignment is strictly based in quantum mechanics. Consider a linear diatomic molecule that is subjected to a moderate intensity laser pulse, tens of  $\text{TW cm}^{-2}$ , which is linearly polarized. The pulse's center frequency is far from an electronic

resonance of the molecule and atomic transitions. In order to simplify the time-dependent Schrödinger equation, the molecule can be modeled in the ridged rotor approximation. The following derivations and equations are based off the work done by T. Seideman *et al.* (1995, 2003, 2006). Some details of the derivations are omitted due to being beyond the scope of this work. For the more rigorous derivation the reader is referred to the work by T. Seideman *et al.* By using the rigid rotor eigenstates, the field-free and field interaction Hamiltonians,  $H_0$  and  $H_{int}$ , can be written in the same form as equation 9 and 10. One can use the reduced operator  $\hat{\rho}(t)$  to rewrite the expectation value in terms of a quantum mechanical trace. After the substitution one would use the quantum Liouville equation (equation 13) to solve for the time evolution. By using the following equations one can obtain a complex set of coupled differential equations.

$$\frac{d\hat{\rho}(t)}{dt} = -\frac{i}{\hbar}[H_0 + H_{int}] + \left(\frac{d\hat{\rho}(t)}{dt}\right)_{dis} \quad (13)$$

$$\left(\frac{d\hat{\rho}(t)}{dt}\right)_{dis} = -\sum_{JM J'M'} \left\{ \begin{array}{l} \frac{1}{2}[K_{JM J'M'} |JM\rangle\langle JM| \hat{\rho}(t)] \\ -K_{JM J'M'} |J'M'\rangle\langle J'M'| \langle JM| \hat{\rho}(t) |JM\rangle \\ +\gamma_{JM J'M'}^{(\rho d)} |JM\rangle\langle JM| \hat{\rho}(t) |J'M'\rangle\langle J'M'| \end{array} \right\} \quad (14)$$

$$\hat{\rho}(t) = \sum_{JM J'M'} \rho_{JM J'M'}(t) |JM\rangle\langle J'M'| \quad (15)$$

$K_{JM J'M'}$  and  $\gamma_{JM J'M'}^{(\rho d)}$  are respectively the population transfer rate and the pure decoherence rate from  $|JM\rangle$  to  $|J'M'\rangle$ . The term  $\left(\frac{d\hat{\rho}(t)}{dt}\right)_{dis}$  describes the evolution of the dissipative part of the density matrix.

Further examination of the resulting matrix presents two terms that constitute  $\langle \cos^2\theta \rangle$ .  $\langle \cos^2\theta \rangle$  is identically equal to  $\langle \cos^2\theta \rangle_p + \langle \cos^2\theta \rangle_c$ .  $\langle \cos^2\theta \rangle_p$  represents the population decay of the molecules. In a dissipative medium this value will return to an equilibrium value of 1/3. This value can be thought of as the baseline value for the amount of alignment.  $\langle \cos^2\theta \rangle_c$  measures the coherence between the revival events. This value will eventually decay to zero due to the decoherence of these events. Thus, once the system returns to equilibrium, the  $\langle \cos^2\theta \rangle$  total value will return to the isotropic value of 1/3. The decay of both of these effects is determined by inelastic collisions [S. Ramakrishna 2006]. For the non-adiabatic alignment, an increase of temperature will decrease the degree of coherence for the rotations and increase the inelastic collisions, leading to reduced alignment.

### 3.5 Experimental Methods and Applications

As the subject of molecular alignment has developed, there has been an array of exciting new experiments and applications. Molecular alignment can be applied to identify different isotopes of the same molecule in a gas in a non-destructive method [S. Fleischer 2008]. The alignment of a molecule has been shown to affect the HHG from a molecule [T. Kanai 2005]. It has been shown that the molecular alignment induced lensing and steering effects can lead to modulation of THz intensities for air based bi-filamentation [M. Durand 2010]. In order to determine the degree of molecular alignment one must measure it. Due to the radically short durations of the alignment actions, the ability of measuring them requires highly sensitive techniques. W. Kim et al. (1996) used Raman spectroscopy on naphthalene trimmers to report the first verification of laser based alignment. Methods such as homodyne techniques [Th. Vieillard 2013, N. Xu 2008], four-wave mixing [S. Fleischer 2008], electron

density and phase measurements [S. Varma 2012] are only able to reconstruct a positive change in  $\langle \cos^2(\theta) \rangle$  from the molecular alignment. By using heterodyne detection techniques [N. Xu 2008], measuring the HHG produced [T. Kanai 2005], and spectral changes dependent on the revival events (figure 14) [F. Calegari 2008], one can probe the negative changes in  $\langle \cos^2(\theta) \rangle$ .

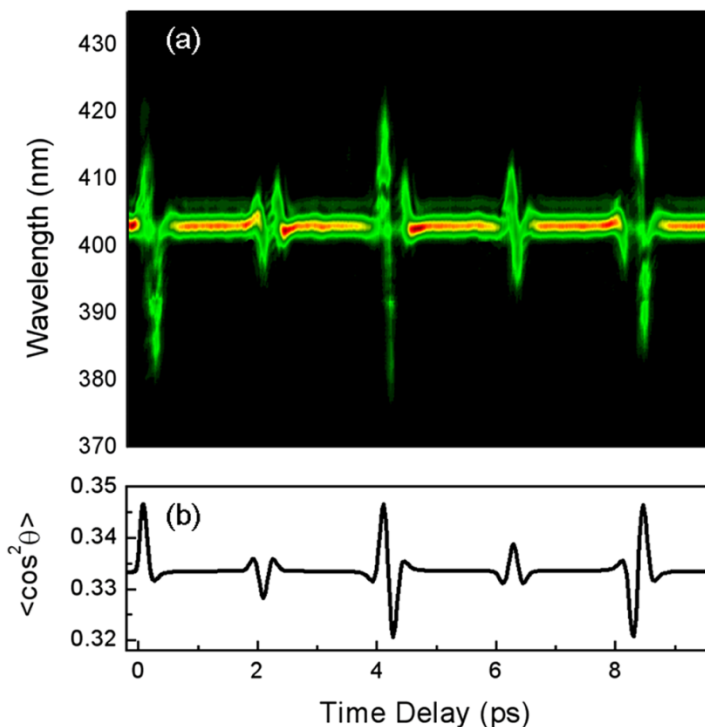


Figure 14. Temporal evolution of the nonadiabatic revival events in  $N_2$ . a) The experimental results from probe spectrum. b) Simulation of the nonadiabatic alignment in  $N_2$  [F. Calegari 2008]

One popular technique is based off photo dissociation and Coulomb explosion [L. Holmegaard 2010, V. Kumarappan 2008, D. Pavičić 2007, K. F. Lee 2004, H. Sakai 1999, H. Stapelfeldt 1998]. A molecular gas is first supersonically expanded into a vacuum chamber. Then the molecules are aligned through static fields, adiabatic, non-adiabatic or any possible combination of the three. The molecules are dissociated by an ultrashort temporal duration

high intensity pulse with circular polarization. Circular polarization is used in order to not influence the alignment of the molecules and the distribution of the molecular fragments. The resulting molecular fragments are accelerated by a weak static electric field towards the detector. Figure 15 shows an example of the molecular fragment measurements. The angular distribution of these fragments is a direct measurement of the alignment and orientation. The molecular-frame photoelectron angular distributions detection has become a standard for investigation of molecular dynamics [L. Holmegaard 2010]. H. Stapelfeldt et al. (1995) reported the first work on femtosecond time resolved measurements of photo dissociation from Coulomb explosion. It was later shown how Coulomb explosion with a femtosecond pulse allowed measurement of both the structure and the dynamics of inter-nuclear wave packets on an angstrom spatial and femtosecond temporal scale [H. Stapelfeldt 1998].

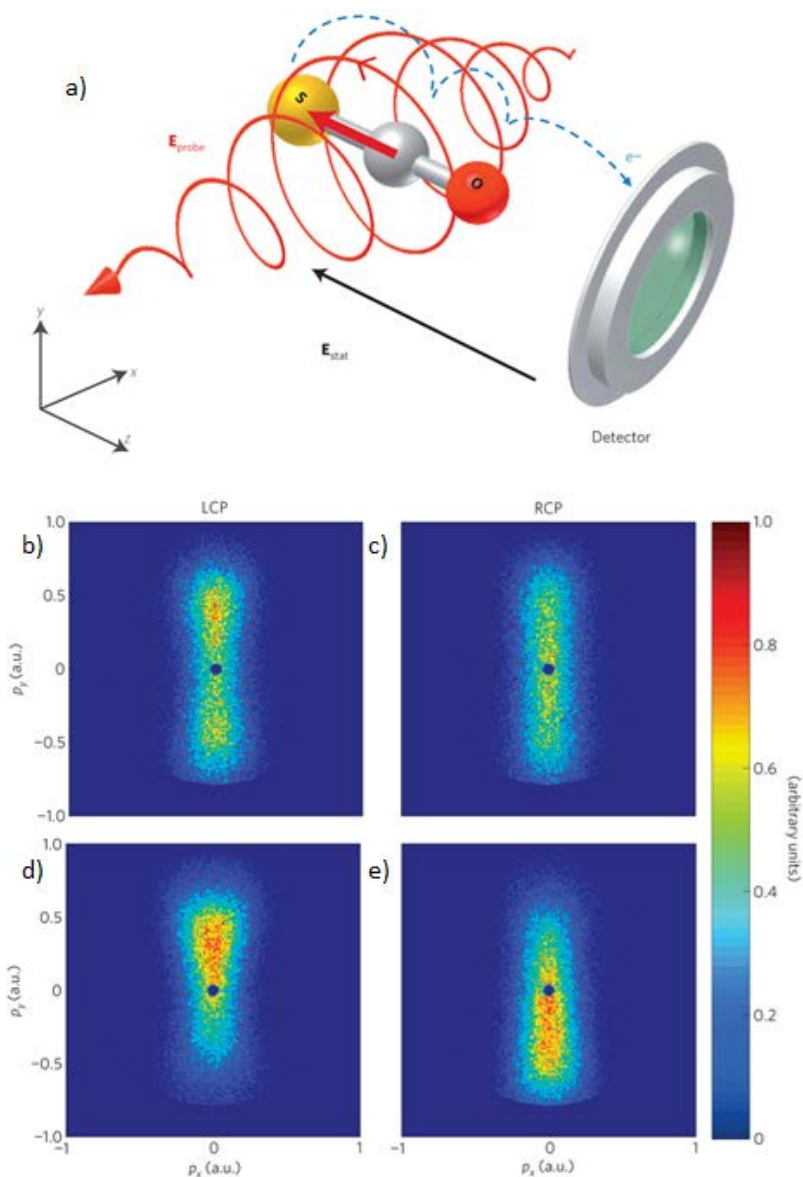


Figure 15. a) Cartoon of the experimental set-up of an OCS molecule oriented with its permanent dipole moment (bold red arrow) pointing in the direction of the static electric field. The left circularly polarized, LCP, probe pulse ionizes the molecule and imparts an upward momentum to the freed electron resulting in recording on the upper part of the detector. b) Two-dimensional momentum image of the electrons from a randomly oriented sample of OCS molecules ionized by the LCP pulse. c) The same as in b) but with a right circularly polarized, RCP, probe pulse. d) and e) are probed the same as b) and c), respectively, but the OCS molecules are oriented perpendicular to the image plane. [L. Holmegaard 2010 ]

The photo absorption/dissociation is dependent on the molecule's axis with respect to the electric field polarization. By controlling the angle of the molecule the light will preferentially populate different energy states and configurations, allowing for state selection



[H. Stapelfeldt 2003]. Due to the importance of ionization for the generation of high harmonics, HHG, it is clear that angular dimension of the molecules is fundamentally important. HHG can be explained using the three step model [J. L. Krause 1992, Z. Chang 2011]. First, an electron tunnels through the potential barrier that is modified by an intense field. Next, the laser field reverses, which drives the freed electron and has a probability of recombining with the initial ion. Finally, if the electron combines with the ion a high energy photon is emitted. By using the pump-probe method T. Kanai et al. (2005) examined how the alignment of CO<sub>2</sub> affected the generation of high order odd harmonics through quantum interference. The commonly used method of pump-probe consists of an initial beam that is split into two pulses. These pulses are delayed from each other temporally. Generally, one pulse modifies and interacts with the sample, and then the delayed second pulse interacts with the aligned medium. By varying the delay between the pulses one can obtain extremely well temporally resolved events.

It has been shown that by illuminating molecules with a second pulse during the field free revival events, the alignment can be enhanced or diminished [K. F. Lee 2004, S. Fleischer 2008]. This ability can be used in differentiating molecules in a mixed gas or even different isotopes of the same molecule, figure 16 [S. Fleischer 2008]. The advantage here is the ability to perform these experiments at room temperature with non-resonant laser sources for all linear symmetric molecule species.

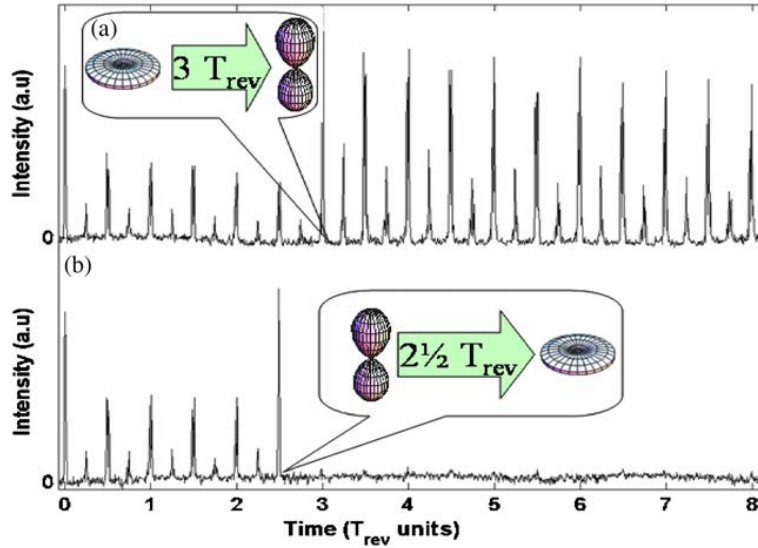


Figure 16.  $^{15}\text{N}_2$  gas alignment signal. a) After the molecules were initially aligned, a second pulse illuminates them at the 3rd revival. The pulse coherently adds to the first one, enhancing the alignment. b) The second pulse arrives at an odd revival event, leading to an annihilation of the field-free alignment. [S. Fleischer 2008]

Filamentation is a highly non-linear process that depends on the linear and non-linear indexes of refraction in addition to the induced ionization and resulting plasma. From understanding this, it is clear to imagine how molecular alignment can affect filamentation. The non-linear Kerr index refraction has two components, the instantaneous electronic motion and the nuclear/molecular response [J.-F. Ripoche 1997]. This statement is only valid for molecules that have anisotropic polarizability, e.g.  $\text{CO}_2$  or  $\text{N}_2$ . Therefore noble gases will only have an electronic Kerr response. J.-F. Ripoche et al. (1997) was able to use the shift of the centroid of a filament's spectrum to examine the temporal evolution of molecular alignment with respect to filamentation. After a filament propagates, the air molecules will undergo periodic revival events due to the nonadiabatic alignment from the filament. A pulse following the filamenting beam will experience spectral broadening at maxima of the rotational revivals [F. Calegari 2008]. Via simulation, the molecular alignment can not only provide an ultra-broad spectrum

but compression for few-cycle pulses as well [J. Wu 2008]. The frequency of a few-cycle pulse undergoing filamentation can be red or blue shifted dependent on the alignment of the revival event [J. Wu 2009]. The molecular rotational revival events can act to enhance or reduce/eliminate filamentation [F. Calegari 2008, S. Varma 2008, Y.Feng 2011]. When the molecules are aligned parallel to the polarization of the electric field,  $\langle \cos^2\theta \rangle > 1/3$ , a probe beam would see the effective index of refraction increase. In the set-up where the molecules and polarization are perpendicular the index of refraction will decrease. The molecular alignment will act analogously to a positive (negative) lens for parallel (perpendicular) alignments [S. Varma 2008, S. Varma 2009, Y.Feng 2011]. In addition to the focusing capabilities, the filament can be steered and enhanced [S. Varma 2008]. M. Durand et al. (2010) were able to show that the molecular lensing and steering effects can lead to modulation of THz intensities for air based bi-filamentation. Using two color filaments, fundamental and second harmonic frequencies, the  $\chi^{(3)}$  of the neutral molecules and laser intensities within the filament were modified, resulting in modulation of the THz emission [T.-J. Wang 2011]. The birefringence effects from filamentation field-free alignment have been shown to be advantageous for HHG due to the tailoring of strong-field phenomena by the polarization pulse shaping [M. Negro 2010]. The plasma density and length have been shown to be affected by the alignment of the molecular axes [S. Varma 2012]. The electron density was shown to increase for alignments with  $\langle \cos^2\theta \rangle > 1/3$  [S. Varma 2012]. Molecular alignment has been shown to affect many facets of filamentation; however through the filamentation process, one should also be able to examine the features of non-adiabatic molecular alignment dynamics.

## 4 EXPERIMENTAL SET-UP

### 4.1 Equipment

#### 4.1.1 Laser

The laser used in this study was the SpectraPhysics Spitfire master oscillator power amplifier, MOPA. This is a CPA system that allows for the generation of ultrashort pulses with high peak powers. The KMLabs oscillator uses Kerr-lens passive mode locking to generate  $\sim 70$  fs pulses with a few nanojoules of energy at tens of MHz. The spectral bandwidth is centered at 810 nm. Before being amplified the pulses are temporally stretched using a Martinez configuration [O. Martinez 1987]. After being stretched to hundreds of picoseconds, the pulse enters the regenerative amplifier. Here the repetition rate is reduced to 1 kHz using a Pockels cell. The pulse is then able to pass through the gain medium many times using an additional Pockels cell. The Ti:Saph crystal is Brewster-cut to allow only the horizontal polarization. As seen in figure 17, the combination of a quarter wave plate, Pockels cell, and Brewster-cut prism, allow a pulse to be amplified from the nJ to the mJ energy level. By adjusting the triggering of the Pockels cells, one has control over the repetition rate and the amplification. After the pulse is amplified by  $\sim 10^6$ , the pulse enters the Treacy compressor [E. Treacy 1969]. The compressor is designed to have the inverse of the dispersion induced by the Martinez stretcher. This allows the pulse to be recompressed, achieving an output pulse that is  $\sim 100$  fs with  $\sim 1$  mJ of energy at 1 kHz repetition rate.

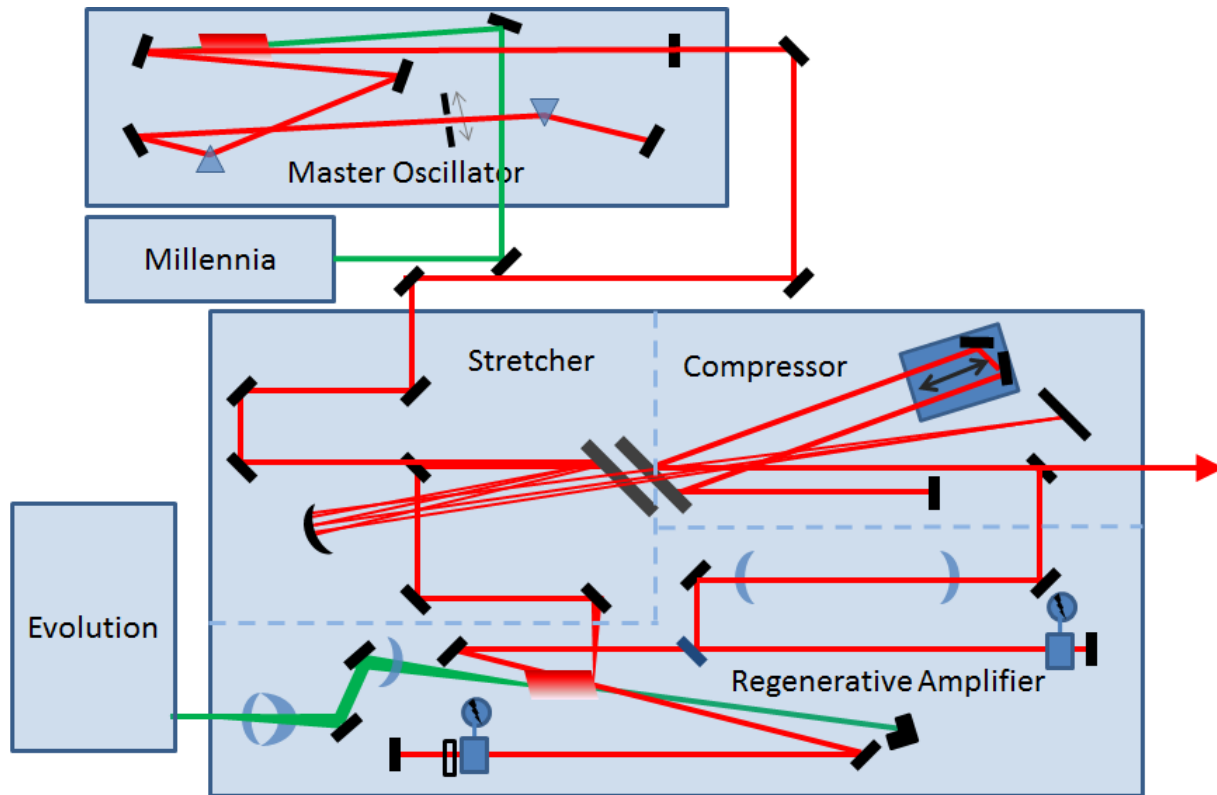


Figure 17. Schematic outline of the SpectraPhysics Spitfire laser

#### 4.1.2 Gas Chamber

The gas chamber used for this study, figure 18, was designed to allow 30 cm – 40 cm of beam propagation in the chamber before self-focusing induced collapse. Both the input and exit windows were made of fused silica with anti-reflection coatings at 800 nm. The windows were AR coated to prevent losing energy from reflections ( $\sim 4\text{-}6\%$  from air to glass incidence due to Fresnel reflections) and protect the optics from the high intensity beam.

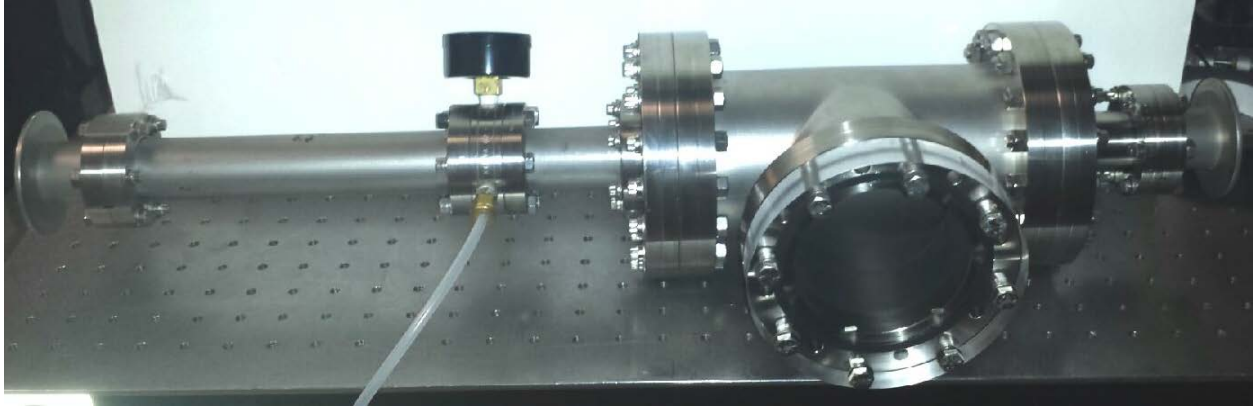


Figure 18. Gas chamber

In order to test the gas chamber's ability to be "air tight", it was pumped down to  $3 \times 10^{-5}$  Torr. The chamber was able to hold vacuum several days after pumping. After the chamber was pumped down, it was filled with 99.8% purity  $\text{CO}_2$  (Air Liquid – "Bone Dry"). For the molecular alignment and filamentation processes it is imperative to confirm that there was no detectable amount of  $\text{N}_2$  in the gas chamber. The spectrum of a filament generated in the gas chamber was measured using an Ocean Optics spectrometer. The resulting spectrum showed that due to the lack CN signatures the chamber did not contain  $\text{N}_2$ , figure 19.

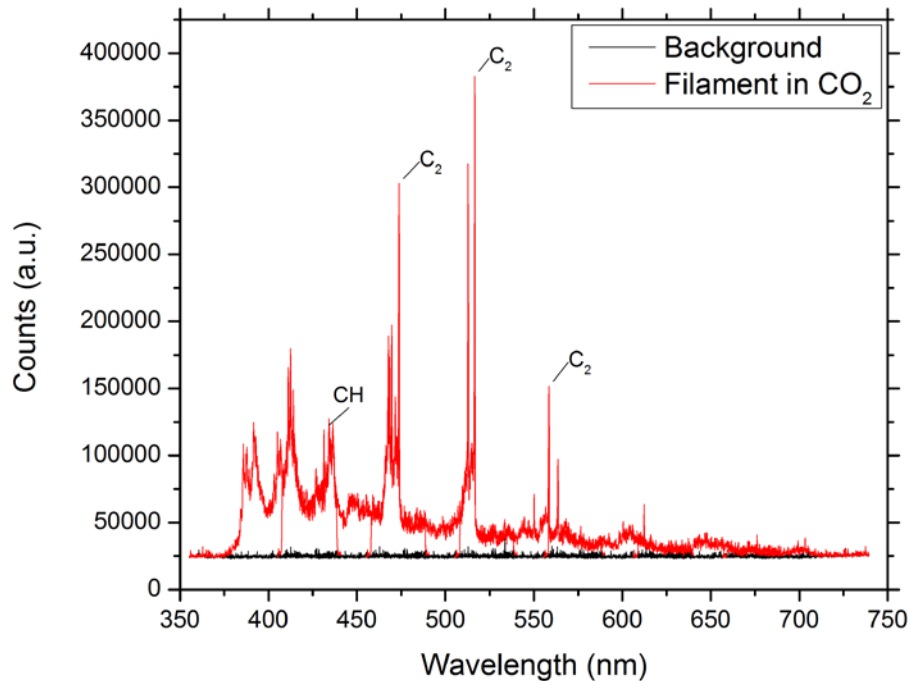


Figure 19. Filament spectrum in 1 atm of  $\text{CO}_2$ . The absence of CN dimers with the Violet band (0-0) transition bandhead at 388.5 nm, indicate that there is not  $\text{N}_2$  in the chamber

## 4.2 Data Collection

### 4.2.1 Pump-Probe Technique

The technique of pump-probe is used to be able to examine phenomena occurring in the ultrafast time regime. A Mach-Zehnder style interferometer was used for our experiment, figure 20. The beam propagates  $\sim 5$  meters from laser to the interferometer. The beam passes through a half-wave plate to control the amount of energy in each polarization. The TE polarization is reflected off the first beam cube to a manual linear delay stage. The TM polarization transmits through the beam cube to an automated linear delay stage. The polarizations are recombined in the second beam cube. The combined beam is reflected off the final mirror to the lens before the gas chamber. The beams were both temporally and spatially

aligned to ensure optimum pulse overlap. The temporal overlap was determined by placing a half-wave plate at the output to rotate both polarizations  $45^\circ$  to allow for interference. After the half-wave plate the beam was reflected off a Brewster angle polarizer. The delay stage was tuned until fringes were observed. The fringes were optimized to obtain the required temporal overlap. The automated linear stage provided 160 ps of usable delay.

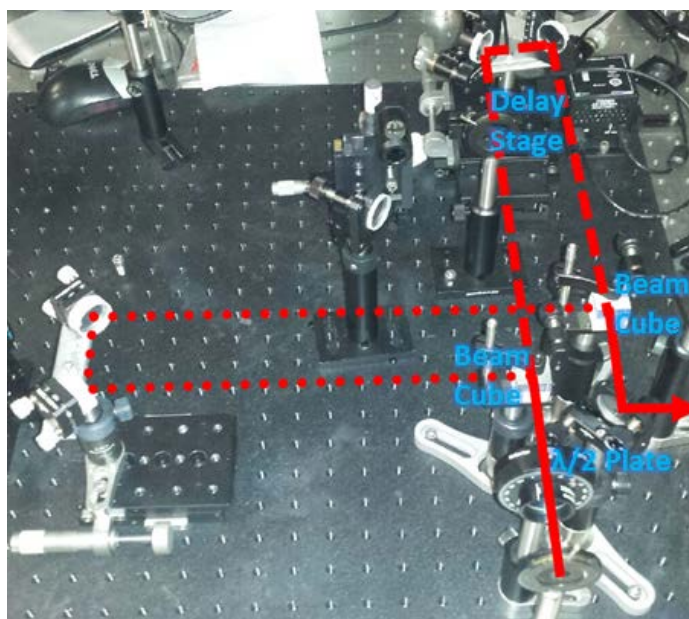


Figure 20. Variable interferometer used for pump-probe method. Circles and dashes correspond to TE and TM polarizations, respectively

In the set-up used (figure 21) the lower energy pump beam was used to align the molecule of  $\text{CO}_2$ . Therefore, the probe beam used was the high energy filamenting beam. In the following chapter, there is a more detailed explanation of the filament probe interaction with the align molecules. By varying the position the automated linear stage the minimum temporal



resolution was 130 fs. The minimum temporal resolution was chosen to match the pulse temporal duration. See appendix for the pulse measurement techniques used.

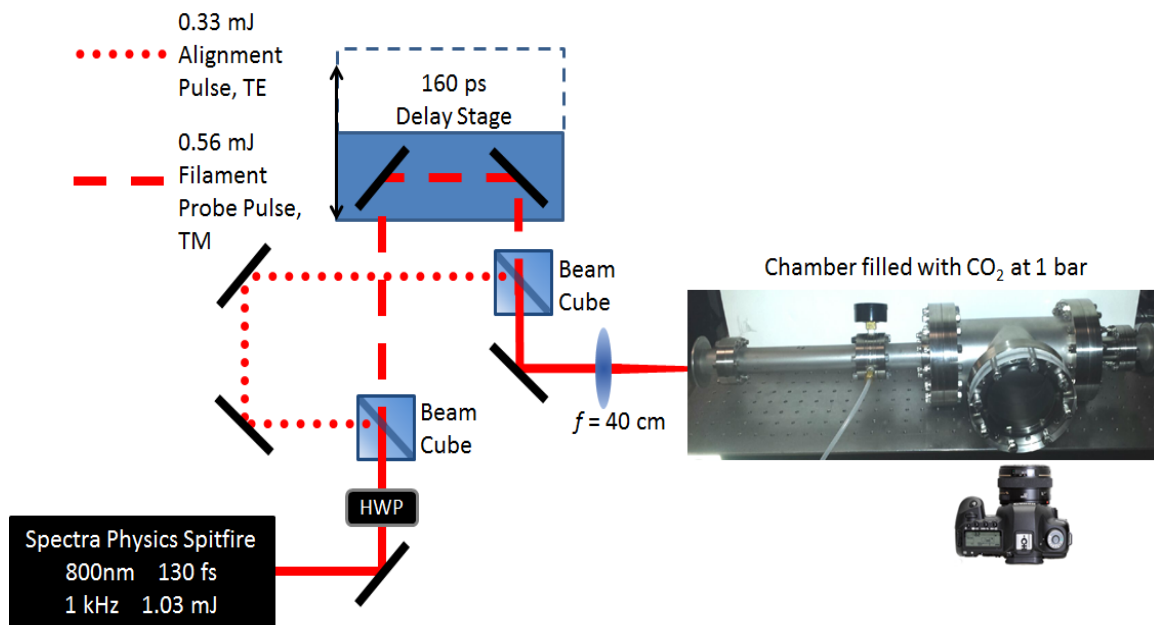


Figure 21. Experimental set-up for filamentation interaction with molecular alignment

#### 4.2.2 Observables Measured

The filament collapse and length were measured by imaging the plasma emission. A commercial SLR camera (Cannon 5D MK2) was used to image the resulting plasma emission from the side of the filament, figure 22. For each delay time for the pump and probe beams five images were taken. By taking several images for each delay it allowed for proper deviation and averaging measurements. The images were taken sequentially rather than repeating a full scan of the delay times. By comparing the first molecular revival events with the data taken it was evident that repeating a full scan was not necessary. Through monitoring the filament

collapse position and plasma column length, non-adiabatic molecular revival events in CO<sub>2</sub> gas were able to be experimentally measured using filamentation.



Figure 22 Example image of the plasma emission from the filament interaction with CO<sub>2</sub>

## 5 FILAMENT INTERACTION WITH ALIGNED CO<sub>2</sub> MOLECULES

### 5.1 Introduction and Motivation

The effects of molecular alignment on filamentation have been documented for several years [J.-F. Ripoche 1997, S. Varma 2008, 2009, 2012, F. Calegari 2008, Y.Feng 2011]. Filamentation is a nonlinear propagation regime, resulting from the dynamics competition between the Kerr effect, leading to the collapse of an intense laser pulse which ionizes the air, and the resulting plasma defocusing. The filament leaves a plasma column, which is 100  $\mu\text{m}$  in diameter, which lasts over several nanoseconds. The plasma can be characterized by its emission spectrum. Using a pre-align gases, one can change the position where the filament starts [Y.Feng 2011], enhance the overall length of the filament [S. Varma 2009], control the distance between two co-propagating filaments [S. Varma 2008], and also control secondary filaments emission such as THz radiation and supercontinuum generation [M. Durand 2010].

The filament length is determined by several coupled complex non-linear mechanisms. These mechanisms are related to, but not limited to, alignment dependent ionization, plasma density, non-linear refractive index (both electronic and molecular contributions), pulse duration/intensity, electric field polarization, diffraction, and dispersion. The alignment of molecules has been shown to affect the plasma density of a gas [S. Varma 2012]. For parallel alignment of the molecular axis and electric field polarization, there was an increase in the plasma density of the filament in air.

The studies of filamentation and molecular alignment have considered how a filament induces molecular alignment and the resulting effects. We propose using a filament as a probe

to investigate the molecular alignment features of a non-ionized aligned medium. The filament interaction with pre-aligned molecules will alter the properties of the filament. In this work, we present proof that laser filamentation can be used as a mean to probe molecular alignment. In this case, we used CO<sub>2</sub> as the medium for molecular alignment. CO<sub>2</sub> is studied due to its long rotational period of 42.7 ps as compared to the period for N<sub>2</sub>, 8.46 ps. This long rotational period could allow one to investigate the effects of inelastic collisions on the temporal dynamics of the aligned molecules.

## 5.2 Theoretical Studies

The theoretical modeling results follow from the nonadiabatic alignment derivation in chapter 3. Figure 23 is a simulation of nonadiabatic alignment in CO<sub>2</sub> by a 19 TW cm<sup>-2</sup>, 132 fs pulse, with a center wavelength at 810 nm, in 1 bar of pressure. The simulation includes all of the collision related dissipate effects. The B<sub>0</sub> of CO<sub>2</sub> is 0.39 cm<sup>-1</sup> and this leads to a theoretical rotational period of 42.7 ps [G. Herzberg 1955]. The first peak in figure 20 is the initial alignment of CO<sub>2</sub>; 42.5 ps later the molecule has completed a full rotation. The revival events for nonadiabatic alignment are a direct consequence of the coherent superposition of the wave packets. As the wave packets temporally interfere the shape of the wave packet will change to a “cigar” shape (for positive changes in  $\langle \cos^2(\theta) \rangle$ ) or a “disk” shape (for negative changes in  $\langle \cos^2(\theta) \rangle$ ), figure 24 [S. Fleischer 2008]. This evolution between “cigar” and “disk” does not pertain to the geometry of molecules; it is the shape of wave packets that are changing. The dashed line in figure 23 is the value of  $\langle \cos^2(\theta) \rangle$ , 1/3, for a random distribution of molecules. At 21.3 ps the CO<sub>2</sub> molecule is at the half rotational period. This half rotational period revival features are inverted from the full rotational period event structure.

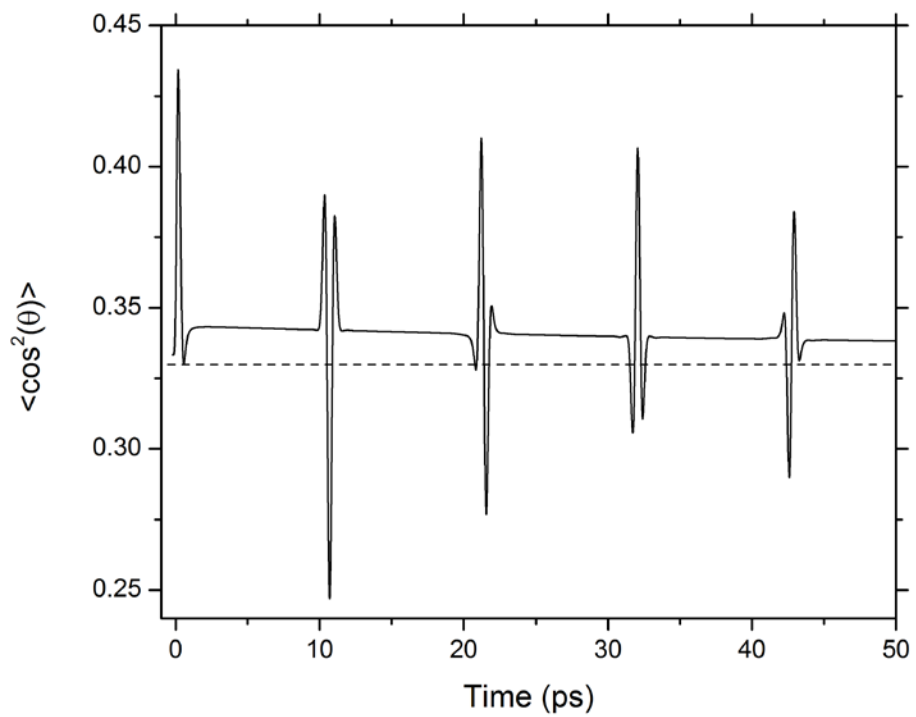


Figure 23. Simulation of nonadiabatic molecular alignment of CO<sub>2</sub> by 19 TW cm<sup>-2</sup> 132 fs pulse, with a center wavelength at 810 nm, in 1 bar of pressure. Simulation by T. Seideman and S. Ramakrishna

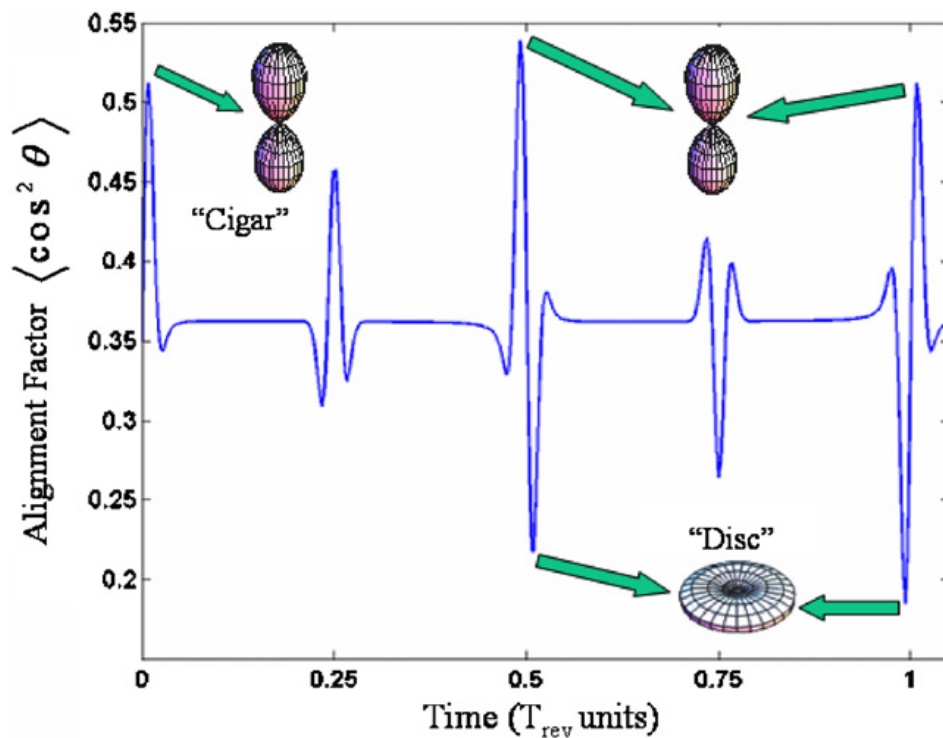


Figure 24. The calculated alignment factor temporal dependence after excitation by a short strong laser pulse. The calculation is performed for  $^{15}\text{N}_2$  at room temperature and atmospheric pressure. At the integer and half-integer multiples of the revival period, the molecular wave packet evolves between alignment (“cigar”) and anti-alignment (“disc”). [S. Fleischer 2008]

By simulating the alignment, we are able to determine the experimental tolerances allowed for the system. The  $\text{CO}_2$  nonadiabatic alignment modeling uses quantum mechanical density matrix formalism. From this, the rotational state-to-state rotation rates resulting from the collisional effects of the molecules were calculated. The simulations were performed using the M-independent, rigid rotor, and energy-corrected sudden (ECS) approximations. ECS law leads to an exact mathematical relationship for an increasing temperature from the decrease of the average duration of the collisions. The collisional dynamics were presumed to be independent of the quantum number, M. M is the projection along the polarization axis of the total angular momentum. Treating the molecules as rigid rotors allows one to neglect the

centrifugal distortion. The alignment revivals are minimally sensitive to centrifugal distortion [J. M. Hartmann 2012]. The molecules of CO<sub>2</sub> are initially at room temperature (296 K), therefore primarily in the ground state. The vibrations of the molecules were disregarded as well. The vibration-translation and vibration-rotation collisional transfers are much slower and less efficient than rotation-rotation and rotation-translation. The vibrational transfer rates of CO<sub>2</sub> are on the order of a nanosecond, whereas the rotational transfer rates are less than ~200 picoseconds [J. M. Hartmann 2012]. All of the simulations were performed by T. Seideman and S. Ramakrishna, from Northwestern University in Evanston, Illinois.

### *5.2.1 Laser Intensity dependence*

We consider a linear molecule, CO<sub>2</sub>, in a dissipative medium, subjected to a linearly polarized moderately-intense laser pulse of short duration. The rotational period (42.7 ps) is much longer than pulse temporal duration (132 fs), and the center frequency of the pulse (810 nm) is lower than the electronic transition frequencies (less than 400 nm). Figure 25 shows the theoretical periodic alignment revivals for CO<sub>2</sub> without any collisional dynamics included and for two different laser irradiances. For all of the simulations we examine the average alignment,  $\langle \cos^2(\theta) \rangle$ , of the molecules. The angle  $\theta$  is the angle between the electric field polarization and molecular dipole. From figure 25, one can clearly see that the amount of alignment increases for higher intensity laser pulses, as expected.

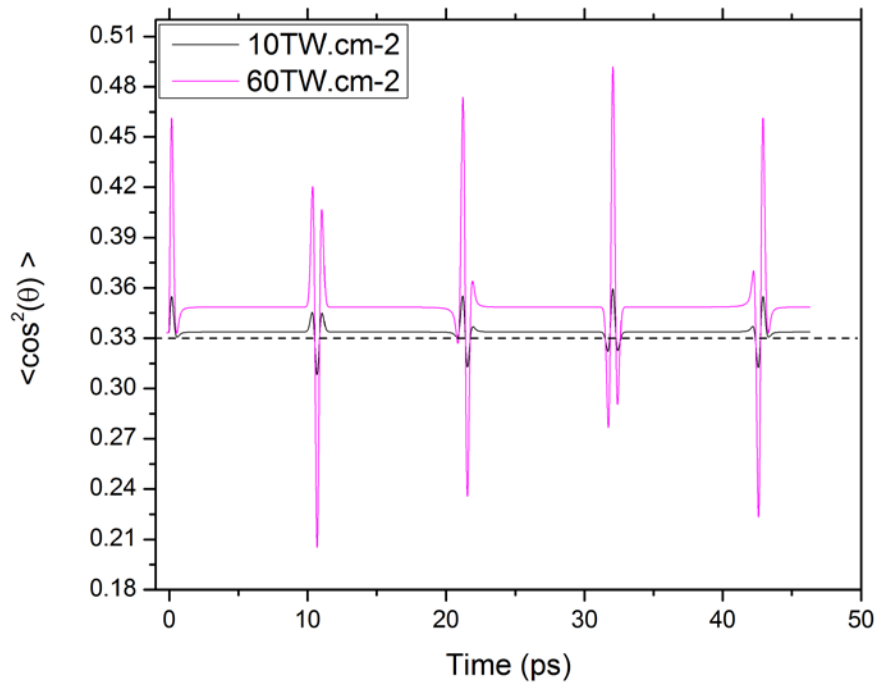


Figure 25. The degree of alignment dependence on different intensities of laser pulses with the same pulse duration

In order to match, the experimental conditions new calculations were made using pulses of 25 and 19 TW cm<sup>-2</sup> and including the collisional dynamics of the CO<sub>2</sub> gas. Figure 26 shows the results from those simulations. Looking at figure 26 b and c, the first and fourth revival events show that  $\langle \cos^2(\theta) \rangle$  is minimally sensitive (change of 0.1) to intensity variations of 6 TW cm<sup>-2</sup> (25 %).



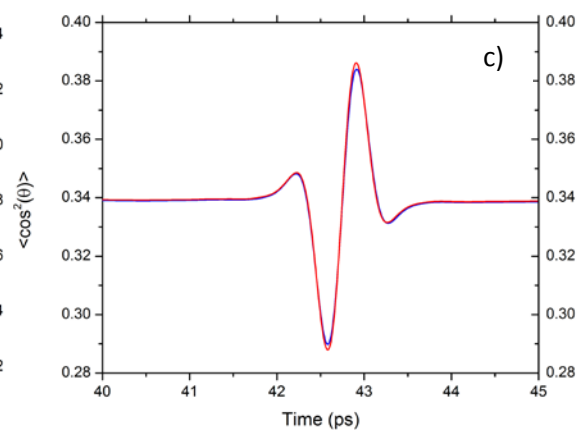
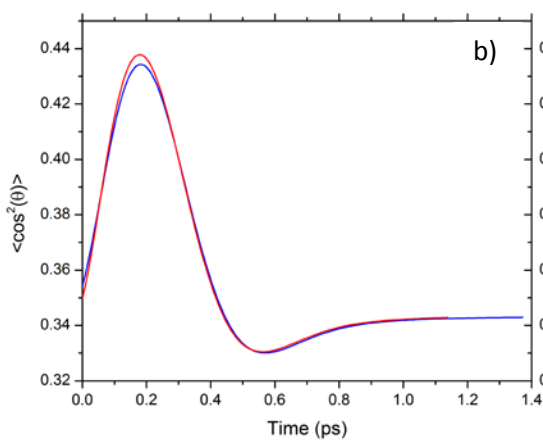
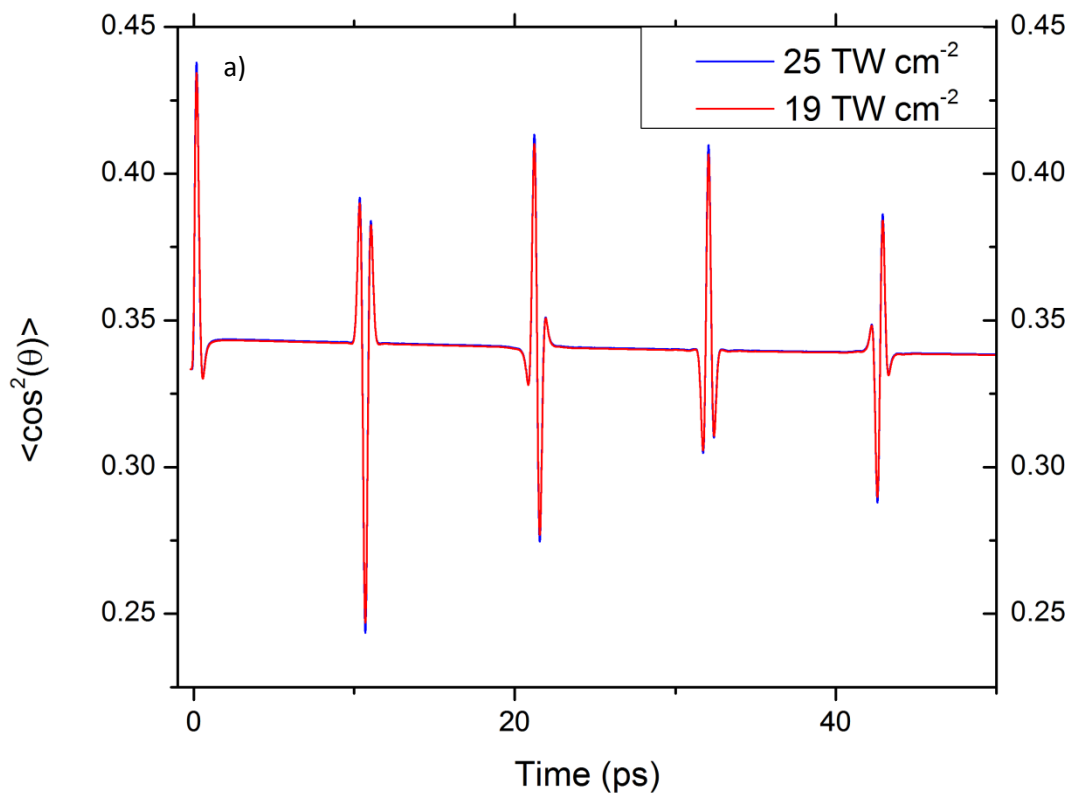


Figure 26. a) Full rotational period free field nonadiabatic alignment dynamics. b) and c) First revival event and fourth revival event, respectively

### 5.2.2 Pressure Dependence

Likewise, slight deviations in pressure did not affect the molecular alignment, as shown in figure 27. It was important to ensure that the alignment was not sensitive to small deviations in pressure due to the fact that the gas chamber did not have an ultra-sensitive pressure gauge. In order to analyze the pressure dependence one must recall that  $\langle \cos^2(\theta) \rangle$  of a gas consist of two terms that are dependent on the collisional dynamics of the system [S. Ramakrishna 2006].  $\langle \cos^2\theta \rangle_p$  is linked to the population decay of the molecules. In a medium at equilibrium the  $\langle \cos^2\theta \rangle_p$  will be equal to 1/3. This value can be thought of as the baseline value for the amount of alignment.  $\langle \cos^2\theta \rangle_c$  measures the coherence between the revival events. As the system returns to equilibrium the  $\langle \cos^2\theta \rangle_c$  value will return to zero.

The alignment period was not affected by different pressures, but the population decay rate was increased, resulting from the higher pressure. This effect can be seen by examining the baselines in between the third and fourth revival events. The relative difference of  $\langle \cos^2(\theta) \rangle$  for the 1.2 bar and 1.0 bar pressures between the third and fourth revivals is only 0.2 %. The effects of pressure for non-adiabatic alignment will be further discussed in the following discussion section.

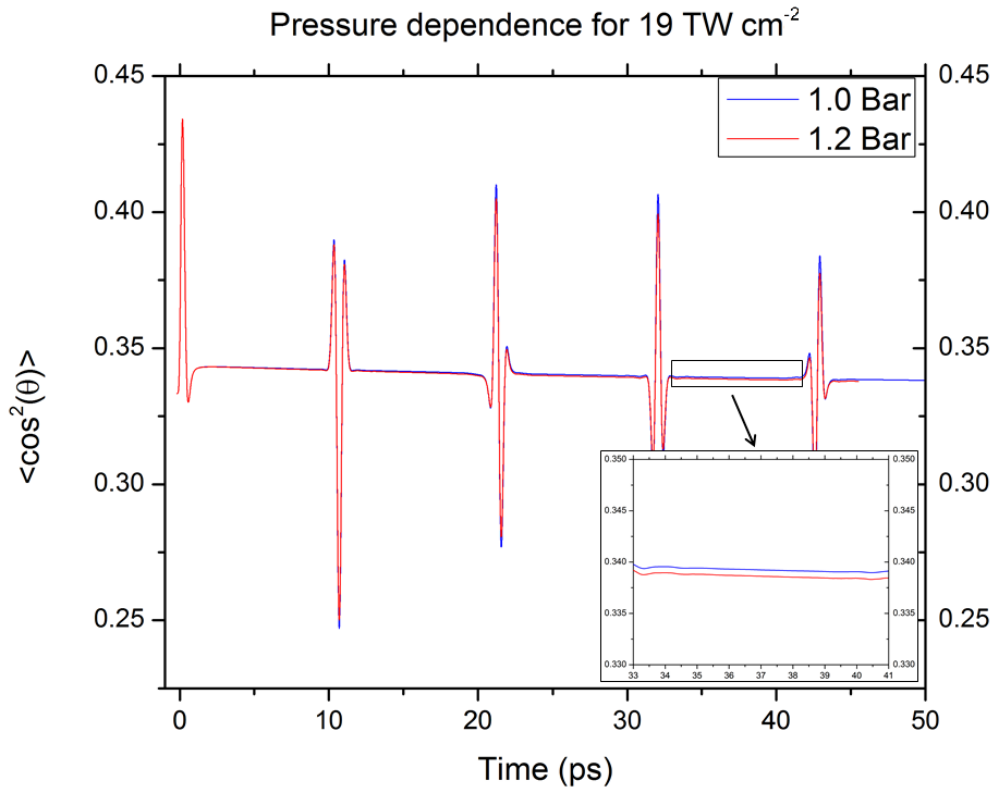


Figure 27. The nonadiabatic alignment pressure dependence for small deviations in pressure

### 5.3 Experimental Results

#### 5.3.1 Filament interaction with an aligned medium

Molecular alignment has been shown to alter many of the features that affect the process of filamentation. By using filamentation, one should thus be able to study the properties of the non-adiabatic molecular alignment dynamics. In the experiment performed the filament was used to probe the alignment features in  $\text{CO}_2$ . The experimental set-up was described thoroughly in chapter 4. The TE polarization had 0.33 mJ of energy and was used to align the  $\text{CO}_2$  molecules. The TM polarization generated the filament to probe the  $\text{CO}_2$  alignment with 0.56 mJ of energy. Both pulses were focused into the gas chamber with a 40 cm

focal length lens. The resulting plasma emission from the filament was imaged using a commercial SLR camera figure 28.

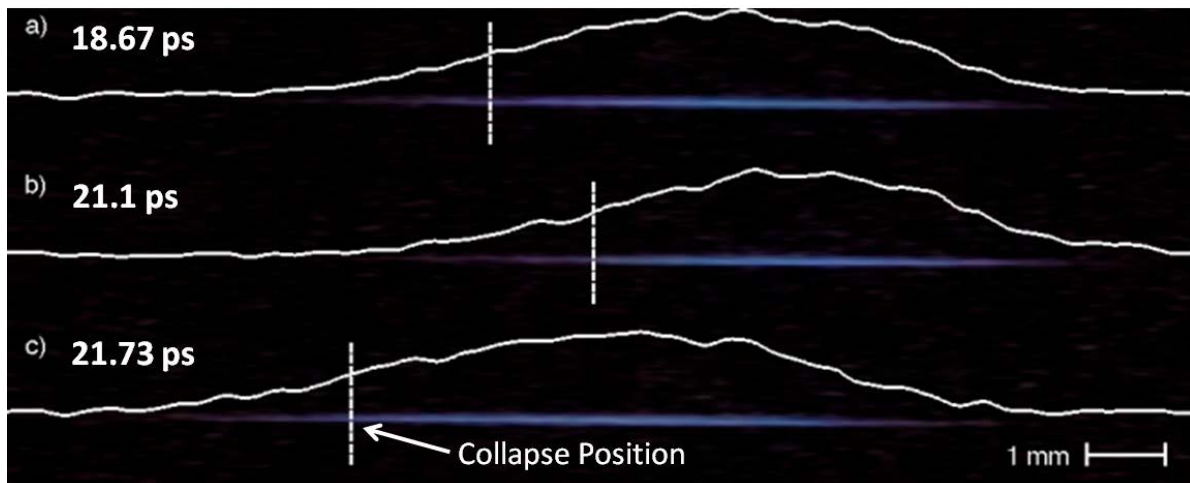
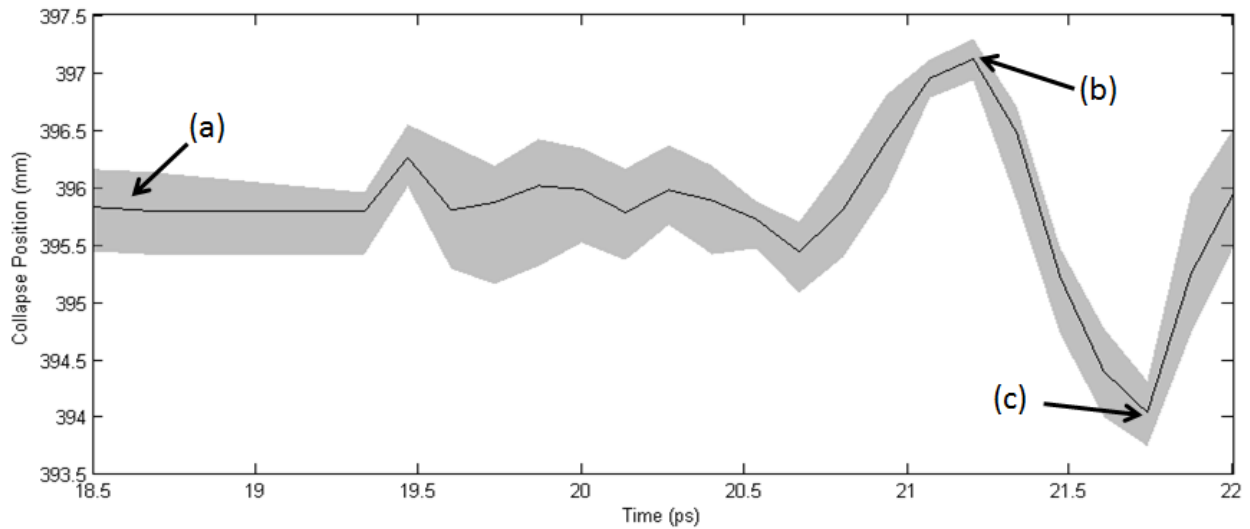


Figure 28. Experimental results of the collapse position and the corresponding images of the filament plasma emission for times about the 3rd revival event. a) The filament in between the second and third alignment events. b) The filament polarization and molecular axis are orthogonal, thus the filament collapses later and the plasma length is decreased. c) The polarization and molecular axis are parallel, resulting in a closer collapse and longer plasma length.

By monitoring the plasma emission image intensity, the collapse position and filament length was recorded. Each of the images' columns was binned to create a 1-D array of values representing the horizontal position and the corresponding pixel intensity. The metric used for the filament collapse position was the first base on the FWHM measurement. The filament length was determined by the entire FWHM of the plasma emission image intensity. The filament collapse position and filament length versus the time delay in respect with the molecular alignment pulse is shown in figure 29. The grey shaded region corresponds to the standard deviation over five images for each time delay measured. The solid black line is the mean value of all of the measurements for each time delay.

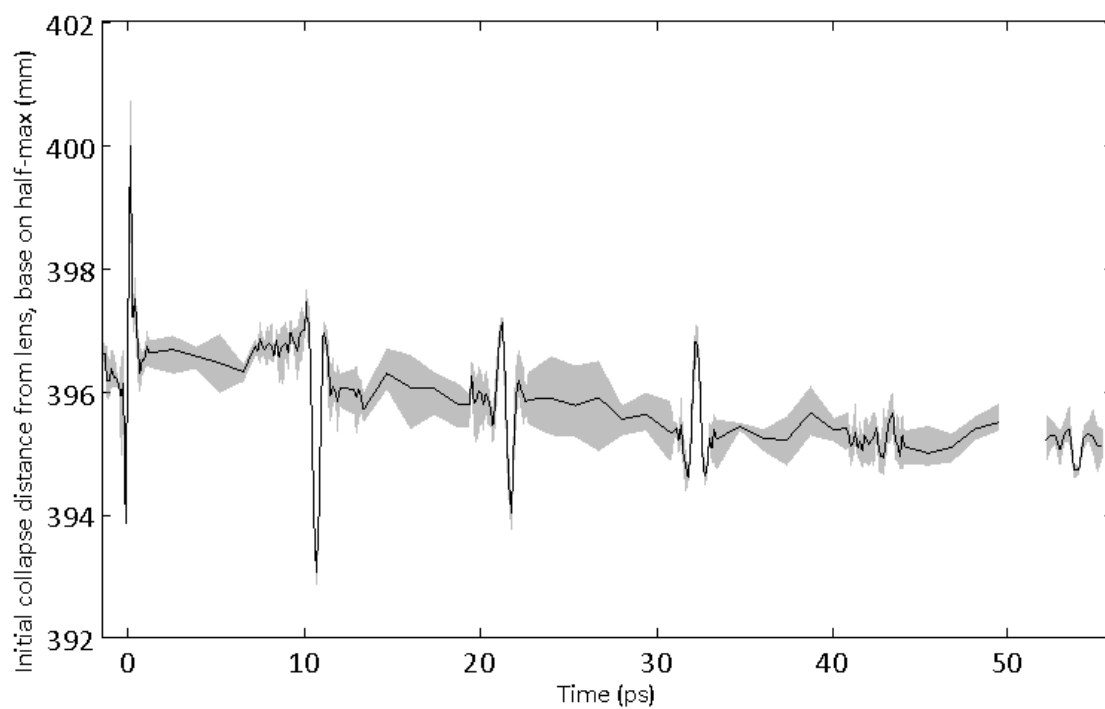
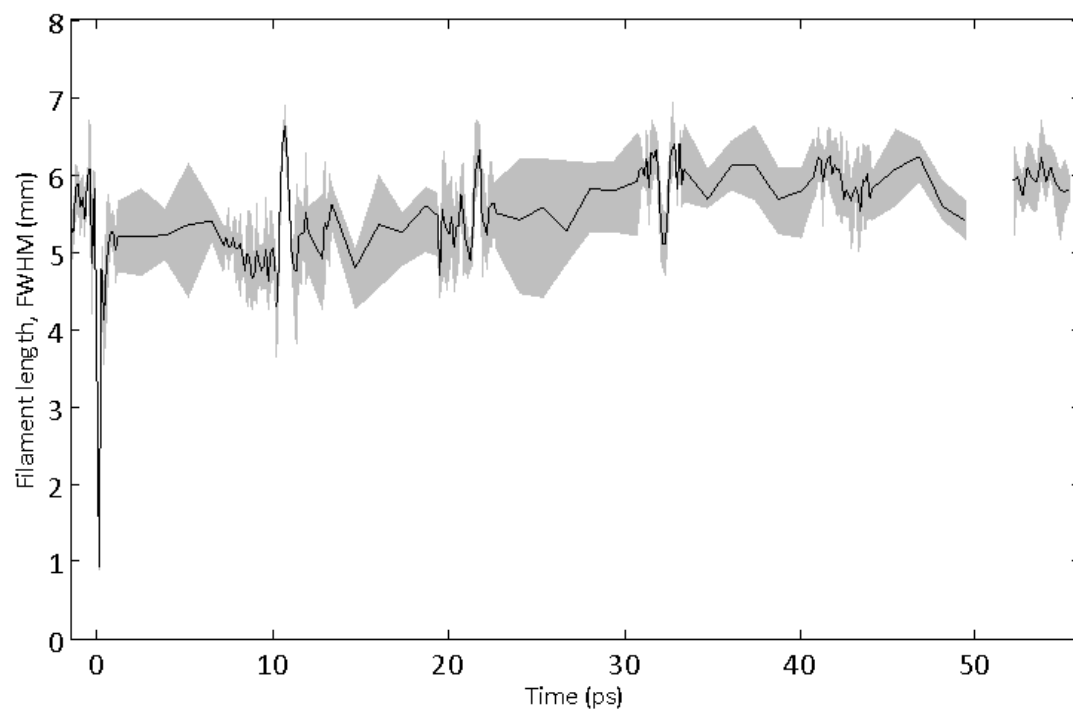


Figure 29. a) The filament collapse position from the lens and b) filament length dependence on the time dependent molecular alignment. The grey shaded region and solid black line correspond to the standard deviation of the measurements taken and the average of the measurements respectively.

Shortly after time zero, the polarization of the filamenting beam and the axis of the molecules are orthogonal, thus the filament collapses furthest from the lens. Whereas at time  $\sim 10.7$  ps, the polarization of the filamenting beam and the molecular axis are parallel, resulting in a collapse closer to the lens. In the case where the molecules are aligned parallel (perpendicular) to the polarization of the probing electric field, the filament will encounter an increased (decreased) refractive index. This increase (decrease) is spatially dependent, thus the refractive index acts as a lens. This lensing effect causes the filament to collapse earlier (later). In the case where the molecules are parallel to the polarization, e.g. time 10.53 ps and 21.73 ps, the molecules act as a converging lens. Comparing the image of the plasma emission in figure 28 and the numerical values of the collapse position in figure 29, one can see the time dependent shift of the collapse position.

#### 5.4 Discussion

The interaction of a filament with nonadiabatically aligned  $\text{CO}_2$  molecules is rich with interesting features. The results of the simulation using the experimental alignment conditions can be seen in figure 30. The simulation models the nonadiabatic alignment of  $\text{CO}_2$  molecules interaction with a pulse 132 fs in temporal duration, intensity of  $19 \text{ TW cm}^{-2}$ , in a gas at 296 K, and 1 bar of pressure. The simulation does not include the effects of the filament interaction with the aligned molecules. In comparing the simulation and the experimental values the period of the events are within the precision of the pulse duration. The simulated  $\langle \cos^2(\theta) \rangle$  and experimental collapse minimum peak of the second revival event happen at times 10.69 ps and 10.53 ps, only a 160 fs difference. The difference in the collapse peak and simulated  $\langle \cos^2(\theta) \rangle$  for the third event is 80 fs. An interesting feature of using a filament probe is that one is able to

obtain the structure of the field free revival events. This ability to reconstruct the features of the simulated nonadiabatic revival temporal dynamics can be seen in figure 30.

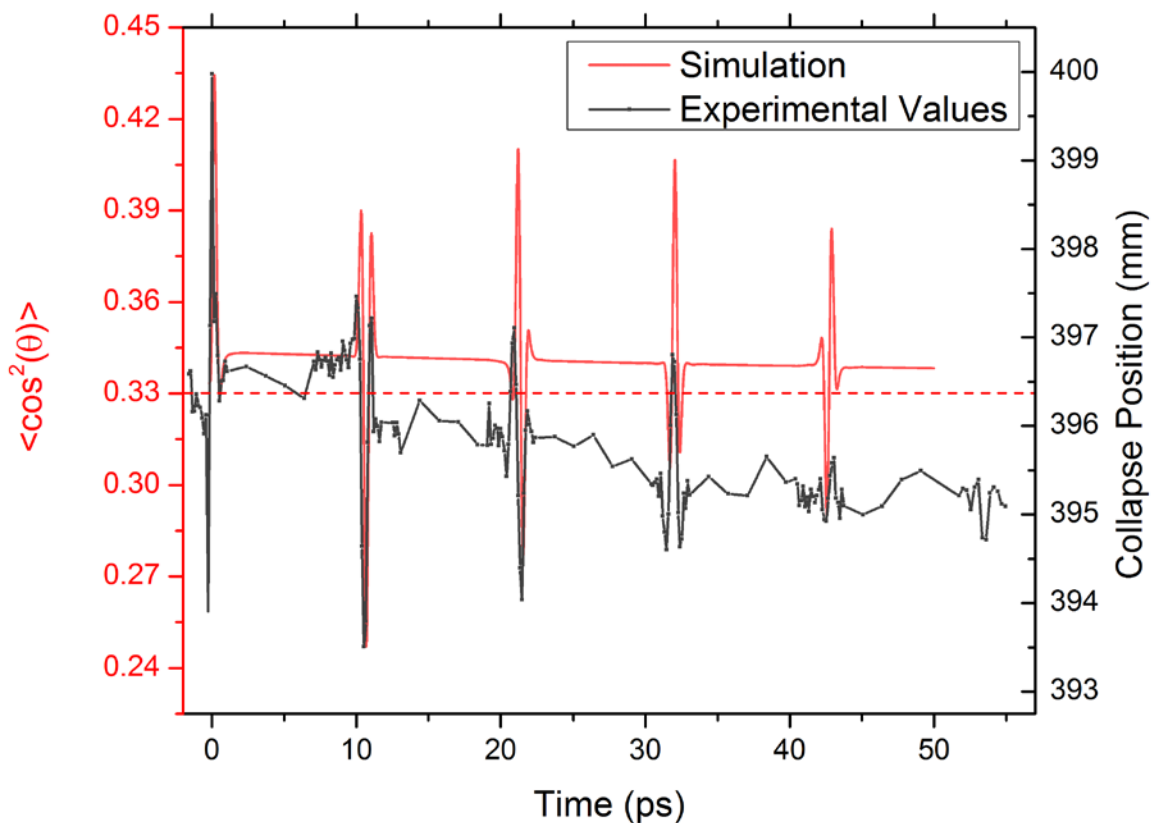


Figure 30. Comparison of the simulated nonadiabatic alignment revival with decay effect included and the experimentally determined molecular alignment revival features

The ability to recover both the positive and negative changes in the revival features is one major advantage of the filamenting probe method. Other methods such as homodyne techniques [Th. Vieillard 2013, N. Xu 2008], four-wave mixing [S. Fleischer 2008], electron



density and phase measurements [S. Varma 2012] are only able to reconstruct a positive change in  $\langle \cos^2(\theta) \rangle$  from the molecular alignment.

As previously discussed, the alignment of the molecules with respect to the polarization of the filament probe allows them to act like a lens. This effect causes the probe pulse to experience an increased index of refraction ( $+\Delta n$ ) focusing the beam, triggering an earlier collapse. For molecules that are orthogonal to the polarization, e.g. time 21.1 ps and 31.87 ps, the molecules have a decreased index of refraction ( $-\Delta n$ ). The decreased index of refraction acts as a diverging lens, increasing the distance for the collapse position. Varma et. al. (2009) showed the ability to use quantum molecular lensing for femtosecond laser filaments.

Figure 31 compares the collapse position, which reconstructs the features of the revival events, and the filament plasma length. The relationship between filament plasma length and molecular alignment can be seen on the second, third, and fourth events. The longer filament plasma emissions correspond to the same temporal delays as the earlier collapse positions. This results from molecular lensing effect due to the locally increased index of refraction. The parallel alignment of the molecular dipole axis and the filament polarization also changes the rate of multiphoton ionization, MPI, for the plasma generation [T. Kanai 2005]. The MPI is reduced in the configuration where the molecules and the filament polarization are orthogonal. Likewise, the shorter plasma emission lengths match the same time as the later collapse positions. These correlate to the locally decreased index of refraction and MPI rates. After the fourth revival event the filament plasma length is not able to clearly characterize the molecular alignment related features. Due to the ambiguity between the filament length and molecular alignment, it was not possible to examine the decay features of the alignment.

The filament length was not able to be a reliable metric of the molecular alignment. The filament plasma length is dependent on several coupled nonlinear effects, e.g. alignment dependent ionization, the plasma density, and the non-linear refractive index (both electronic and molecular contributions). An interesting corollary of CO<sub>2</sub> alignment has been the MPI rate dependence on alignment. The unintuitive maximum peak of MPI was theoretically [S.-K. Son 2009] and experimentally [D. Pavicic 2007] determined to be at 40°. This presents even more complexity to the filament's plasma dynamics.

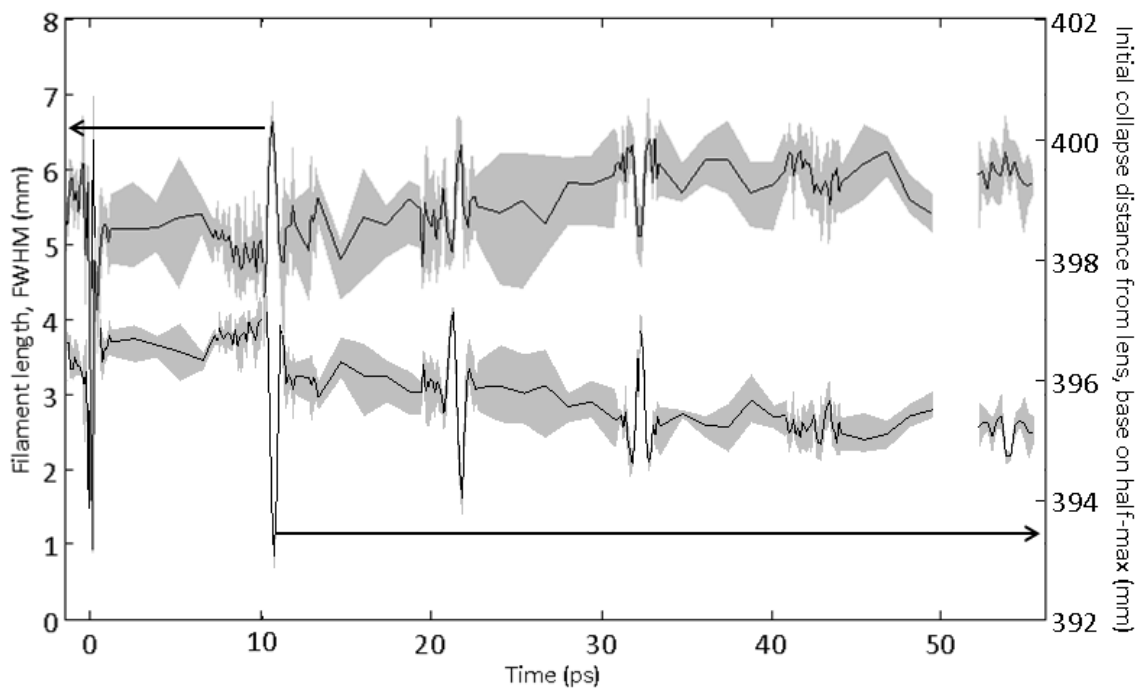


Figure 31. Comparison of the filament length and the collapse position molecular alignment dependence

#### 5.4.1 Population Decay and Coherence

One of the advantages of studying CO<sub>2</sub> molecules, over N<sub>2</sub> or O<sub>2</sub>, is its long rotational period of ~42 ps versus their 8.3 and 11.6 ps rotational periods respectively. The long rotational period allows one to investigate both the population decay and the revival events coherence of the nonadiabatic alignment. The metric for the amount of alignment,  $\langle \cos^2\theta \rangle$ , consist of the two components  $\langle \cos^2\theta \rangle_p$  and  $\langle \cos^2\theta \rangle_c$ .  $\langle \cos^2\theta \rangle_p$  is related to the population decay of the molecules.  $\langle \cos^2\theta \rangle_p$  in a gas at equilibrium will have a value of 1/3. This value is the baseline value for the amount of alignment.  $\langle \cos^2\theta \rangle_c$  measures the coherence between the revival events.  $\langle \cos^2\theta \rangle_c$  is zero when a medium is in equilibrium. The decay rates for both of these factors are governed by the system's inelastic collisions [S. Ramakrishna 2006].

Analyzing the simulations allows one to extract the decay rates for both population decay and the coherence decay rate between the revival events. By ignoring the revival events one is able to study the population decay. The theoretically determined population decay rate observed,  $\tau_p$ , leads to a nearly exponential decay rate. The decay rate was determined by fitting the baseline with an exponential decay. From examining the simulation baseline,  $\tau_p$  of the CO<sub>2</sub> molecules was found to be 64.2 ps. This result is in agreement with the published M-independent theoretical work by Th. Vieillard (2013) and J.-M. Hartmann (2012). In order to compare the population decay, the revival events were removed from the experimental results. The remaining averaged baseline was fit with an exponential decay to compare it to the theoretical result, figure 32. From the experimental data, the population decay rate was determined to be  $33.3 \pm 8.4$  ps. The experimental decay rate is nearly half of the theoretically determined decay rate. There are several factors that may have led to the factor ~2 mismatch.

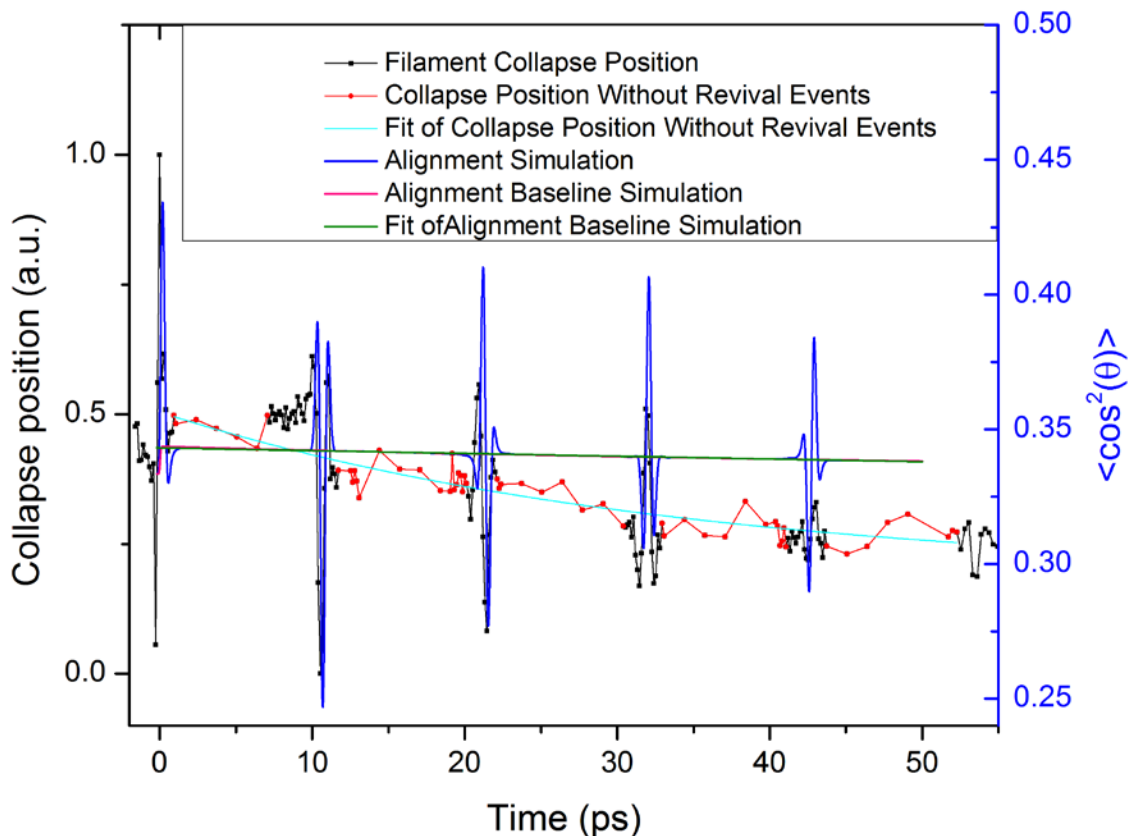


Figure 32. Comparison of the theoretical population decay and experimental collapse position decay

It was expected that the experimental results would decay faster due to the dissipative effects of the plasma. The collision rates used for  $\text{CO}_2$  were from empirical data. The collision rates used in the simulation come from experimental results in much less dissipative environments. Also, the simulation did not take into account the anisotropic ionization for  $\text{CO}_2$ . For a better experimental determination of the population decay more revival events can be probed. It may be possible to investigate revivals up to  $\sim 150$  ps [J.-M. Hartmann 2012]. The number of revival events that can be measured, regardless of the method, is dependent on the time scale of the system to return to equilibrium. Equilibrium conditions are obtained after about 1 ns for  $\text{CO}_2$  [J.-M. Hartmann 2012].

The other component of the total  $\langle \cos^2\theta \rangle$  is linked to the coherence between the revival events. The dynamics from the laser induced nonadiabatic alignment result from the dephasing and rephasing of the rotational coherences. They were determined by the time evolution of the off-diagonal terms of the density matrix [S. Ramakrishna 2006]. This led to a coherence decay rate of 58 ps. Note that the population and decoherence rates are similar, 64 and 58 ps, for the simulation. This similarity is expected from an M-independent calculation [Th. Vieillard 2013].

The decoherence rate was not able to be determined from the experimental results. It may have been possible to extract information about the coherence if later revival events were also measured. It has been recommended that high density/pressure studies could allow one to obtain information on the population decay and decoherence effects independently [S. Ramakrishna 2006, Th. Vieillard 2013]. The disadvantage of a high density study is that the M-independent model is no longer valid. Comparing the M-independent and M-dependent theories of nonadiabatic alignment of CO<sub>2</sub> at 20 bar the M-independent theory fails to reproduce experimental data, figure 33 [Th. Vieillard 2013]. Therefore, the computation of the simulations would have to include the M-dependence to be of use at high pressure. Experimentally, a high pressure environment would yield an increased index of refraction. This increase would support filamentation at much lower energies. The high density thus may impose a limit to the intensity used to align the molecules without ionization.

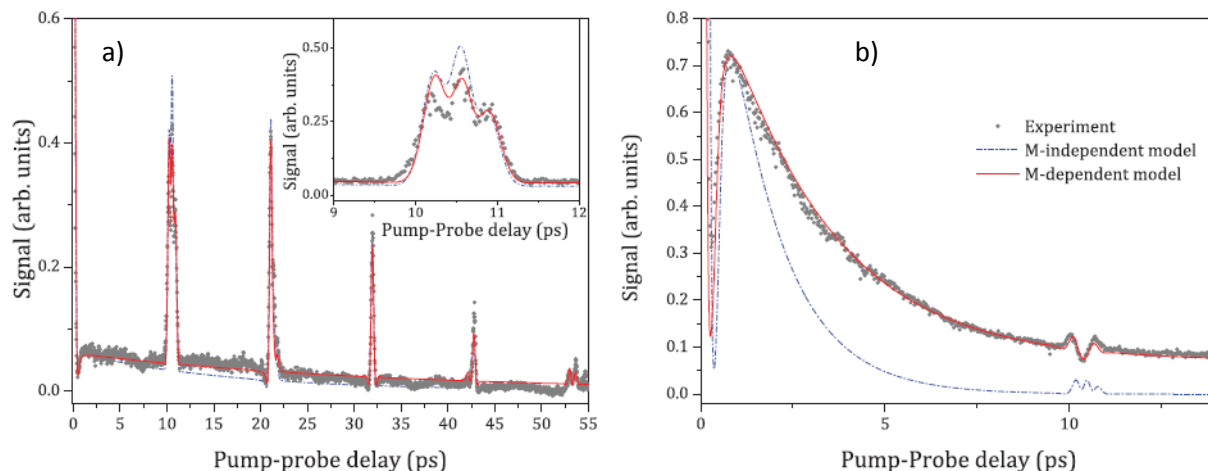


Figure 33. The gray dotted curves are the experimental homodyne signals of the pump-probe measurement in CO<sub>2</sub> at 295 K. The red curve is the M-dependent model and the blue dash-dotted curve is the M-independent model. a) 2 bar with a peak intensity of 45 TW cm<sup>-2</sup>. The insert shows the features of the first revival. b) 20 bar with a peak intensity of 35 TW cm<sup>-2</sup>. [Th. Vieillard 2013]

## 5.5 Conclusion

In this work, we have showed that laser filamentation can be used to probe the molecular nonadiabatic alignment dynamics in CO<sub>2</sub> gas at atmospheric pressure. Through theoretical analysis it has been determined that the alignment dynamics are not highly sensitive to small deviations in pressure ( $\pm 0.1$  bar) and alignment pulse intensity (25% difference in intensity). The changes in pressure resulted only in a very minor change in the population decay rate of the alignment.

The experimental results confirm that our method can reproduce the molecular alignment dependent effects from existing works [S. Varma 2008, 2009, 2012, S. Ramakrishna 2006, S. Fleischer 2008, J.-M. Hartmann 2012, Th. Vieillard 2013]. The index of refraction can be locally modified leading to molecular lensing. By having the molecular dipole axis and the electric field polarization parallel (perpendicular), the molecules will increase (decrease) the

index of refraction. This modification will cause the molecules to act as a converging (diverging lens). This effect leads to a measurement of a filament collapse position that is closer (further) from the lens than that of a filament in randomly aligned molecules.

The correlation between the experiment and theoretical results show that both M-independent theory can be used at atmospheric pressure to determine the alignment structures without collisional effects and that a filament is a reliable probe to reproduce the alignment structures. From the simulation the population decay and the coherence of the revival events decay rates were determined to be 64 and 58 ps, respectively. By analyzing the molecular alignment dependent filament collapse position, the population decay rate was calculated to be  $33.3 \pm 8.4$  ps. This 2-fold mismatch between the theoretical and experiment value stems from the dissipative effects from plasma that were not included in the nonadiabatic alignment model. The MPI alignment dependent rates of CO<sub>2</sub> may have also contributed to the disagreement in population decay rates.

In order to have a better model of the nonadiabatic alignment with a filament probe, the simulation should include M-dependence and the dissipative effects from plasma. Incorporating a split-step Fourier method of modeling filament propagation with the M-dependent molecular alignment theory one should be able to obtain the complete dynamics of a filament interaction with an aligned medium.

## 6 CONCLUSION

The use of femtosecond filamentation as a probe for nonadiabatic molecular alignment has been demonstrated in this work to be an effective measurement technique. It has been shown to be a robust method, with a simple experimental set-up, to obtain information about the structure of field-free alignment revival events. The application of understanding the temporal dynamics of molecules extends beyond the interactions with ultrafast laser pulses. This information would be applicable to any mechanism that is dependent on the molecular alignment.

Through the collaborative efforts with Tamar Seideman and Sai Ramakrishna at Northwestern University, we were able to correlate theoretical simulations of nonadiabatic alignment with experimental measurements of a filament collapse position. By determining the acceptable experimental tolerances for the alignment dynamics, it was found that small deviations in pressure ( $\pm 0.1$  bar) and alignment pulse intensity (25% difference in intensity) did not contribute to a significant change in the outcomes. Both the simulation and experimental results were able to reproduce the theoretical rotational period of CO<sub>2</sub>,  $42.76 \pm 1$  ps. The features of the revival events were able to be reconstructed by the alignment dependence of the filament collapse position. The timing of the revival events matched for the experimental and simulated values within the temporal error of the experimental conditions.

The rates of decay of the population (baseline) alignment and coherence of the phase relationship between revival events were determined by modeling the temporal dissipative dynamics from inelastic collisions. From the simulation, the population decay ( $\langle \cos^2(\theta) \rangle_p$ ) and



coherence dephasing ( $\langle \cos^2(\theta) \rangle_c$ ) rates were calculated to be 64 and 58 ps, respectively. The experimentally determined value of the alignment population decay rate was  $33.3 \pm 8.4$  ps. The population decay rate was approximately half the theoretical value. The offset of the two values can be traced to the limit of the simulation, as it only modeled the nonadiabatic alignment, not the filament interaction with aligned molecules. The plasma is significantly more dissipative than non-ionized gases, because of the higher temperature and the large electronic density, leading to collisions. These plasma effects were not included in the nonadiabatic alignment model since the collision rates used come from empirical data in much less dissipative environments. In addition to the dissipative effects, the model does not account for the alignment dependent multiphoton ionization.

### 6.1 Outlook and Future Work

In order to have a better understanding of femtosecond filamentation interaction with aligned molecules, the model must be improved. The simulation should include the M-dependent effects and the dissipative effects from plasma. By incorporating a split-step Fourier method of modeling filament propagation with the M-dependent molecular alignment theory, one should be able to better reconstruct the dynamics of the interaction of aligned molecules with a filament.

The information about the population decay and coherence dephasing in  $\text{CO}_2$  could be improved by increasing the number of revival events measured, i.e. measuring 2-4 full rotational periods. Aiming at investigating the decoherence effects, this technique should be studied in high density environments. However, the increased pressure decreases the energy required to ionize the air. The high density thus may impose a limit to the intensity that can be

used to align the molecules without ionization. One method to avoid this potential problem would be to use a pulse with a lower frequency to align the molecules, e.g. a pulse with a center wavelength greater than 1  $\mu\text{m}$ . This method could utilize a two color pump-probe technique, where the alignment pulse is of a lower frequency than the filamenting probe pulse.

The technique of using a filament as a probe for molecular alignment should be expanded to other gases. For example, a filament should be used to measure the nonadiabatic molecular alignment of  $\text{N}_2$ . The constants of  $\text{N}_2$ , that are pertinent for filament propagation in air, are well known. The benefit of that study is that one could directly link filament propagation with the dynamics of nonadiabatic molecular alignment. Understanding the interaction of femtosecond filamentation with aligned molecules will allow for spatial and temporal tailoring of the filament propagation.

## **APPENDIX: PULSE MEASUREMENT TECHNIQUES**

## **Pulse Temporal Duration Measurement**

Ultra-fast physics and optics requires one to know, with high precision, the pulse duration and energy of the laser used for the light matter interactions. For all of the experiments performed the laser's pulse duration was measured with both a Swamp Optics GRENOUILLE and an in-house built single shot autocorrelator.

### **GRENOUILLE**

The GRENOUILLE, GRating-Eliminated No-nonsense Observation of Ultrafast Incident Laser Light E-fields, is a pulse measure technique based off the FROG, Frequency-Resolved Optical Gating. The major differences in the FROG and the GRENOUILLE include the FROG using a thin second harmonic generation, SHG, crystal and spectrometer, whereas the GRENOUILLE uses a thick SHG crystal and a camera [P. O'Shea 2001]. The GRENOUILLE is far less sensitive to alignment, but is still able to provide phase and intensity information about the pulse.

The beam is aligned into the GRENOUILLE, which uses a beam splitter to split the beam into two pulses. Through the use of cylindrical lens, the pulses are passed through the SHG providing a single shot autocorrelator measurement in the horizontal plane. The vertical plane will contain the wavelength distribution due to the crystal's angle sensitive phase matching conditions. This vertical spread of the components of the spectrum allows the camera to act as a spectrometer. By combining the data from the vertical and horizontal plane, the GRENOUILLE is able to extract the phase information [P. O'Shea 2001].

## Autocorrelator

The GRENOUILLE has been claimed to measure pulses as low as  $\sim 50$  fs accurately, but for pulses with durations below  $\sim 50$  fs another method is required [P. O'Shea 2001]. Our experience has led the need for another method of confirmation for the temporal pulse duration, even for pulses  $>50$  fs. An in-house single shot autocorrelator, the Erikolater, was built to simultaneously solve these problems. In order to greatly reduce any additional dispersion and pulse broadening, it was designed to not require the use of lenses. The only transmission optics used was a 50/50 beam splitter and the SHG BBO, beta barium borate, crystal. Following the path of the beam in figure 34, first the beam is divided via a 50/50 beam splitter. One pulse is reflected off the beam splitter, and then reflected off four turning mirrors directing it into the BBO. The transmitted pulse propagates to a linear translation stage then to a turning mirror that allows for tuning of the crossing angle of the two beams. The linear translation stage is used to ease the temporal alignment of the pulses. Using the angle tuning mirror and the following mirror the beams are crossed into the BBO crystal. As the beams propagate through each other temporally in the crystal, a spatial phase matched second harmonic frequency is produced. In order to remove the fundamental 800 nm signal, a filter is placed in front of a CCD camera to reject the 800 nm light. The doubled frequency is then imaged on to the camera.

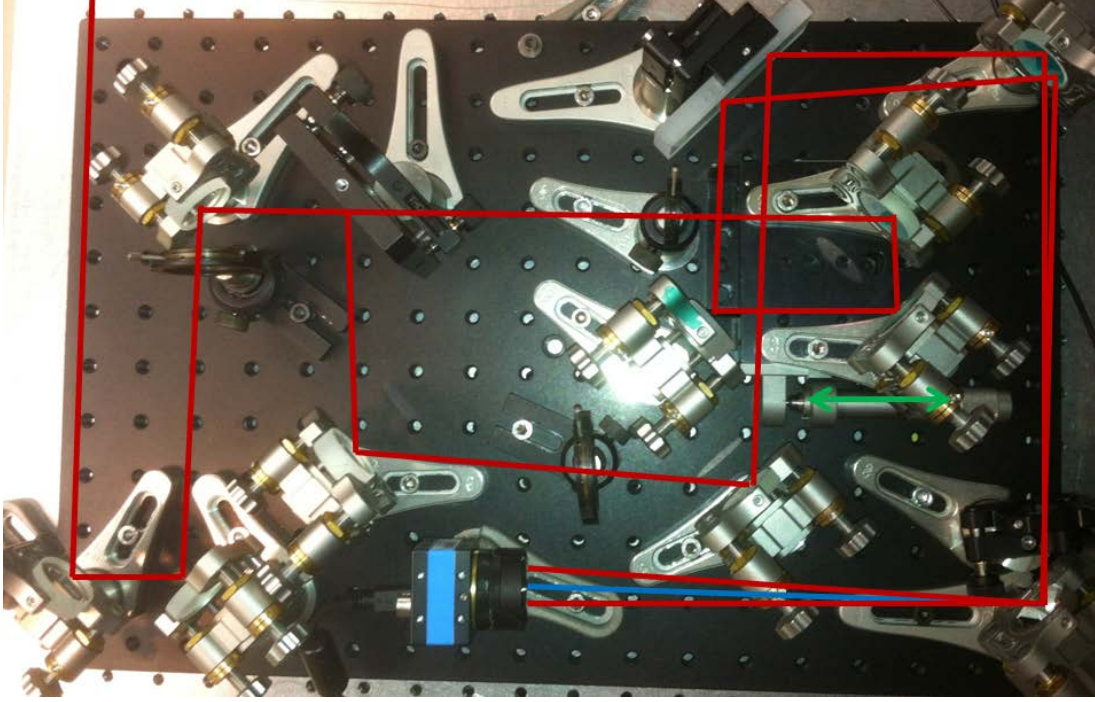


Figure 34. Erikolater. Pulse duration measurement experimental set-up

From the resulting image from the camera (figure 35) one can determine the pulse duration. The temporal window of observation,  $\tau_{obs}$ , is determined by the crossing angle,  $\varphi$ , and the diameter of the BBO crystal, equation 16. The temporal resolution,  $r_{AC}$ , will then be dependent on the observation window and the number of pixels of the camera.

$$\tau_{obs} = \frac{n*d*\sin(\frac{\varphi}{2})}{c} \quad (16)$$

$$r_{AC} = \frac{\tau_{obs}}{\#of\ pixels} \quad (17)$$

$$\tau_{pulse} = \frac{\tau_{AC}*r_{AC}}{K} \quad (18)$$

$\tau_{AC}$  is the full width half max of the autocorrelation trace in pixels. From equation 18, one can calculate the pulse duration, assuming a deconvolution factor  $K \approx 1.35$  for a Gaussian pulse [D.

Herrmann 2010]. The FWHM used was computed by summing the pixels in each column and taking the value from that summation.

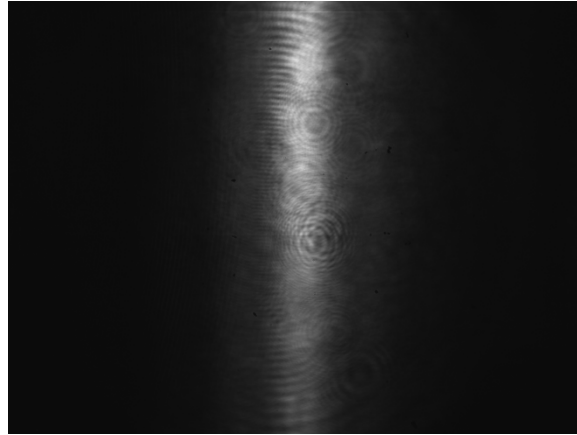


Figure 35. Image from the Autocorrelation

In order to compare both pulse measurement techniques, they were used to measure the pulse duration of the LPL MTFL system. First, the distance between the compressor gratings was optimized to generate the shortest pulse using the GRENOUILLE. This process was repeated using the autocorrelator. By comparing the two methods, figure 36, both methods provided similar traces of the pulse autocorrelation. The autocorrelator and GRENOUILLE measured pulse durations of  $43.7 \pm 1$  fs and  $43.4 \pm 2$  fs.

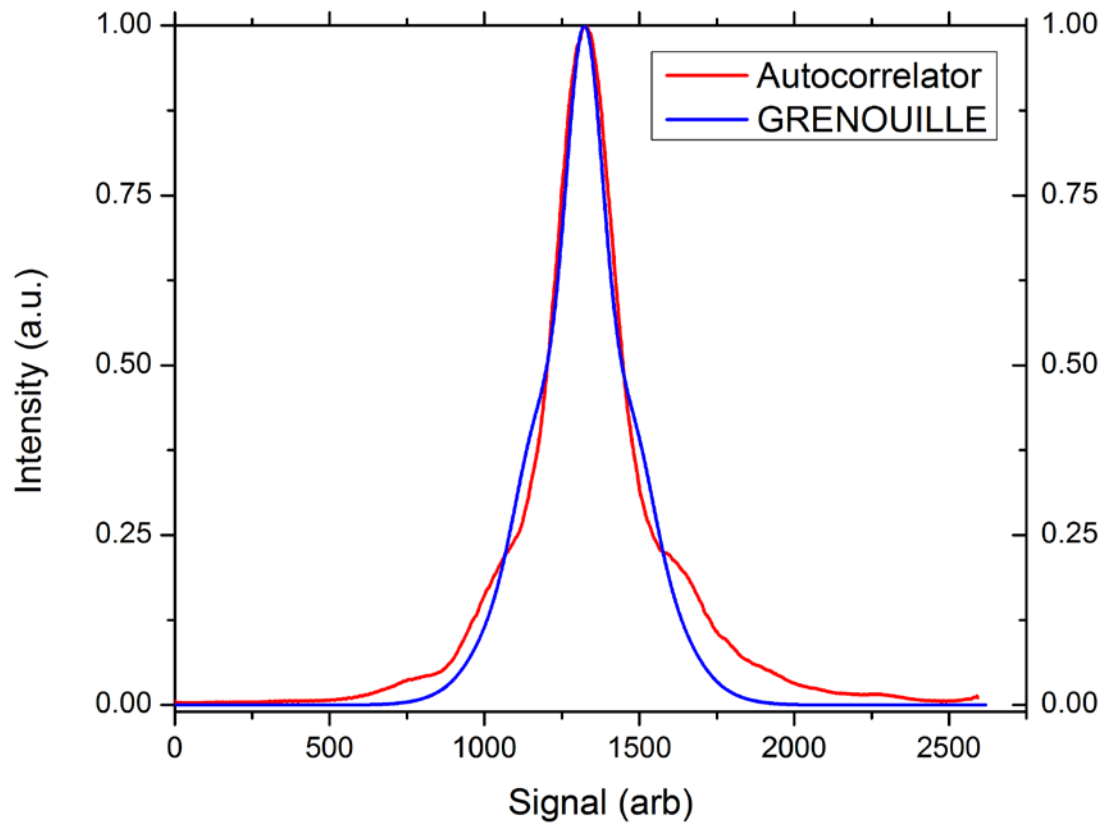


Figure 36. Comparison of the autocorrelator and GRENOUILLE on the MTF system



## LIST OF REFERENCES

- N. Aközbek, A. Becker, M. Scalora, S.L. Chin, C.M. Bowden, *Appl. Phys. B.*, 77 177 (2003)
- N. Aközbek, S. A. Trushin, A. Baltuška, W. Fuß, E. Goulielmakis, K. Kosma, F. Krausz, S. Panja, M. Uiberacker, W. E. Schmid, A. Becker, M. Scalora, M. Bloemer, *New J. Phys.*, 8, 177, (2006)
- M. Alshershby, Z. Hao, J. Lin J., *Phys. D Appl. Phys.*, 45, 265401 (2012)
- J. B. Anderson, R. P. Andres, J. B. Fenn, *Adv. Chem. Phys.*, 10, 275 (1966)
- V. Aquilanti, D. Ascenzi, M. de Castro Vítors, F. Pirani, D. Cappelletti, *J. Chem. Phys.* 111, 2620 (1999)
- N. Barbieri, M. Weidman, G. Katona, M. Baudelet, Z. Roth, E. G. Johnson, G. Siviloglou, D. N. Christodoulides, M. C. Richardson, *Journ. Opt. Soc. Am. B*, 28, 1462 (2011)
- T. Bartel, P. Gaal, K. Reimann, M. Woerner, and T. Elsaesser, *Opt. Lett.* 30, 2805 (2005)
- A. Braun, G. Korn, X. Liu, D. Du, J. Squier, G. Mourou, *Opt. Lett.*, 20, 73 (1995)
- H. Cai, J. Wu, X. Bai, H. Pan, H. Zeng, *Opt. Lett.*, 35, 49 (2010)
- F. Calegari, C. Vozzi, S. Gasilov, E. Benedetti, G. Sansone, M. Nisoli, S. De Silvestri, S. Stagira, *Phys. Rev. Lett.*, 100, 123006 (2008)
- Z. Chang, *Fundamentals of Attosecond Optics*, CRC Press (2011)
- Y.H. Chen, S. Varma, T. M. Antonsen, H.M. Milchberg, *Plasma Phys.*, 1008, 1642 (2010)
- C.-C. Cheng, E. M. Wright, J. V. Moloney, *Phys. Rev. Lett.*, 87, 213001 (2001)
- S. Chidangil, A.K. Dharmadhikari, K. Alti, J.A. Dharmadhikari, D. Mathur, *Journal of Biomedical Optics* 12, 20510 (2007)
- D. J. Cook, R. M. Hochstrasser, *Opt. Lett.* 25, 1210 (2000)

C. Cornaggia, Ph. Hering, Phys. Rev. A, 62, 023403 (2000)

A. Couairon, A. Mysyrowicz, Phys. Reports, 441, 47 (2007)

C. D'Amico, A. Houard, M. Franco, B. Prade, A. Mysyrowicz, Phys. Rev. Lett. 98, 235002 (2007)

C. D'Amico, A. Houard, S. Akturk, Y. Liu, J. Le. Bloas, M. Franco, B. Prade, A. Couairon, V. T. Tikhonchuk, A Mysyrowicz, New J. Phys., 10, 013015 (2008)

J. Dai, J. Liu, X. C. Zhang, IEEE Quant. Elect., 1, 1, (2010)

P. Debye, Chem. Catalog Company, Inc. (1929)

M. Durand, K. Lim, V. Jukna, E. McKee, M. Baudalet, A. Houard, M. Richardson, A. Mysyrowicz, A. Couairon, Phys. Rev. A, 87, 043820 (2013)

J. R. Dwyer, Geophys. Res. Lett., 30, 2055, (2003)

E. Esarey, C. B. Schroeder, W. P. Leemans, Rev. Mod. Phys. 81, 1229–1285 (2009)

D. Faccio, A. Averchi, A. Couairon, M. Kolesik, J.V. Moloney, A. Dubietis, G. Tamosauskas, P. Polesana, A. Piskarska, P. Di Trapani, Opt. Exp., 15, 13077 (2007)

Y. Feng, H. Pan, J. Liu, C. Chen, J. Wu, H. Zeng, Opt. Exp., 19, 2852 (2011)

G. Fibich, B. Ilan, Phys. Rev. E., 67, 3 (2003)

S. Fleischer, I. Sh. Averbukh, Y. Prior, J. Phys. B: At. Mol. Opt. Phys., 41, 074018 (2008)

B. Friedrich, D. R. Herschbach, Nature (London) 353, 412 (1991)

B. Friedrich, D. R. Herschbach, Z. Phys., 18, 153 (1991)

D. J. Griffith, Introduction to Quantum Mechanics, Prentice Hall (1995)

T. Grow, A. Ishaaya, L. Vuong, A. Gaeta, Opt. Exp., 14, 5468 (2006)

K. Guo, J. Lin, Z. Hao, X. Gao, Z. Zhao, C. Sun, B. Li, Opt Lett., 37, 259 (2012)

H. Haberland, U. Buck, M. Tolle, Rev. Sci. Instrum. 56, 1712 (1985)

M. Härtelt, B. Friedrich, *J. Chem. Phys.* 128, 224313 (2008)

J.-M. Hartmann, C. Boulet, *J. Chem. Phys.*, 136, 184302 (2012)

D. Herrmann, R. Tautz, F. Tavella, F. Krausz, L. Veisz, *Opt. Exp.*, 18, 4170 (2010)

G. Herzberg, *MPm. SOC. R. Sci. Liege*, 15, 291 (1955)

L. Holmegaard, J. L. Hansen, L. Kalhøj, S. L. Kragh, H. Stapelfeldt, F. Filsinger, J. Küpper, G. Meijer, D. Dimitrovski, M Abu-samba, C. P. J. Martiny, L. B. Madsen, *Nature Physics*, 6, 428 (2010)

T. Kanai, S. Minemoto, H. Sakai, *Nature* 435, 470-474 (2005)

N. Karpowicz, X.-C. Zhang, *Phys. Rev. Lett.* 102, 093001 (2009)

K. Y. Kim, A. J. Taylor, J. H. Glowina, and G. Rodriguez, *Nat. Photon.* 2, 605 (2008)

W. Kim, P. M. Felker, *J. Chem. Phys.*, 104, 1147 (1996)

M. Kolesik, E.M. Wright, A. Becker, J.V. Moloney, *Appl. Phys. B*, 85, 4, 531 (2006)

M. Kolesik, G. Katona, J.V. Moloney, E.M. Wright, *Appl. Phys. B*, 77, 2, 185 (2003)

J. L. Krause, K. J. Schafer, K. C. Kulander, *Phys. Rev. Lett.* 68, 3535 (1992)

M. Kress, T. Löffler, S. Eden, M. Thomson, H. G. Roskos, *Opt. Lett.* 29, 1120 (2004)

Z. Kudyshv, M. Richardson, N. Litchinitser, *Nat. Comm.*, 4, 2557 (2013)

V. Kumarappan, L. Holmegaard, C. Martiny, C. B. Madsen, T. K. Kjeldsen, S. S. Viftrup, L. B. Madsen and H. Stapelfeldt, *Phys. Rev. Lett.*, 100, 093006 (2008)

B. La Fontaine, D. Comtois, C. Chien, A. Desparois, F., Genin, G. Jarry, T. Johnston, J. Kieffer, F. Martin, R. Mawassi, H. Pepin, F. A. M. Rizk, F. Vidal, C. Potvin, P. Couture, H. P. Mercure, *J. Appl. Phys.* 88, 610 (2000).

K. F. Lee, I. V. Litvinyuk, P. W. Dooley, M. Spanner, D. M. Villeneuve, P. B. Corkum, J. Phys. B: At. Mol. Opt. Phys., 37 (2004)

S. B. Leonov, A. A. Firsov, M. A. Shurupov, J. B. Michael, M. N. Shneider, R. B. Miles, N. A. Popov, Phys. Plasmas, 19,123502 (2012)

M. Liao, W. Gao, T.i Cheng, X. Xue, Z. Duan, D. Deng, H. Kawashima, T. Suzuki, Y.Ohishi, Appl. Phys. Express, 6, 032503 (2013)

W. Liu, S.L. Chin, Opt. Exp., 13, 5750 (2005)

W. Liu, A. Becker,N. Aközbek, C.M. Bowden, S.L. Chin, Opt. Comm., 202, 189 (2002)

G. Luther , A. C. Newell, J. V. Moloney, E. M. Wright, Opt. Lett., 19, 789 (1994)

P. Maioli, R. Salamé, N. Lascoux, E. Salmon, P. Béjot, J. Kasparian, J.-P. Wolf, Opt. Exp., 17, 4726 (2009)

J. H. Marburger, Prog. Quant. Elect., 4, 35 (1975)

O. Martinez, Quant. Elect., 23, 59 (1987)

E. Matsubara, K. Yamane, T. Sekikawa, M. Yamashita, JOSA B, 24, 985 (2007)

G. Méchain, C.D'Amico, Y.-B. André, S. Tzortzakis, M. Franco, B. Prade, A. Mysyrowicz, A. Couairon, E. Salmon, R. Sauerbrey, Opt. Comm., 247, 171 (2005)

G. Millot, J. Chem. Phys., 93, 8001 (1990)

G. Mourou, D.Strickland, Opt Comm., 56, 219 (1985)

M. Negro, C. Vozzi, F. Calegari, S. De Silvestri, S. Stagira, Opt. Lett., 35, 1350 (2010)

E. T. J. Nibbering, P. F. Curley, G. Grillon, B. S. Prade, M. A. Franco, F. Salin, A. Mysyrowicz, Opt. Lett., 21, 62 (1996)

- Y. Nomura, H. Shirai, K. Ishii, N. Tsurumachi, A. A. Voronin, A. M. Zheltikov, T. Fuji, *Opt. Exp.*, 20, 24741 (2012)
- N. A. Panov, O. G. Kosyreva, A. Savel'ev-Trofimov, D. S. Uryupina, I. A. Perezhogin, V. Makarov, *Quant. Elect.*, 41, 160 (2011)
- D. Parker, R. B. Bernstein, *Annu. Rev. Phys.*, 40, 561 (1989)
- D. Pavičić, K. F. Lee, D. M. Rayner, P. B. Corkum, D. M. Villeneuve, *Phys. Rev. Lett.* 98, 243001 (2007)
- H. Pepin, D. Comtois, F. Vidal, C. Y. Chien, A. Desparois, T. W. Johnston, J. C. Kieffer, B. La Fontaine, F. Martin, F. A. M. Rizk, C. Potvin, P. Couture, H. P. Mercure, I. Gallimberti, *Phys. Plasmas* 8, 2532 (2001)
- Y. Petit, S. Henin, W. Nakaema, P. Béjot, A. Jochmann, S. D. Kraft, S. Bock, U. Schramm, K. Stelmaszczyk, P. Rohwetter, J. Kasparian, R. Sauerbrey, L. Wöste, J. Wolf, *Phys. Rev. A*, 83, 013805 (2011)
- S. Ramakrishna, T. Seideman, *J. Chem. Phys.*, 124, 034101 (2006)
- Y. Ren, M. Alshershby, J. Qin, Z. Hao, J. Lin, *J. Appl. Phys.* 113, 094904 (2013)
- J.-F. Ripoche, G. Grillon, B. Prade, M. Franco, E. Nibbering, R. Lange, A. Mysyrowicz, *Opt. Comm.*, 135, 4, 310 (1997)
- J. Rothenberg, *Opt. Lett.* 17, 583 (1992)
- H. Sakai, C. P. Safvan, J. J. Larsen, K. M. Hilligsøe, K. Hald, H. Stapelfeldt, *J. Chem. Phys.* 110, 10235 (1999)
- C. Santhosh, A. K. Dharmadhikari, K. Alti, J. A. Dharmadhikari, D. Mathur, *J. Biomed. Opt.* 12, 020510 (2007)

H. Schillinger, R. Sauerbrey, Appl. Phys. B, 68, 4, 753 (1999)

T. Seideman, J. Chem. Phys., 103, 7887 (1995)

A. E Siegman, Lasers, University Science Books, (1986)

S.-K. Son, S.-I. Chu, Phy. Rev., 80, 011403 (2009)

H. Stapelfeldt, E. Constant, H. Sakai, and P. B. Corkum, Phys. Rev. A 58, 426 (1998)

H. Stapelfeldt, E. Constant, P. B. Corkum, Phys. Rev. Lett., 74, 3780 (1995)

H. Stapelfeldt, T. Seidman, Rev. Mod. Phys., 75, 543 (2003)

H. Takahashi, S. Hasegawa, Y. Hayasaki, App.Opts., 46, 5917 (2007)

F. Théberge, W. Liu, P. Simard, A. Becker, S. Chin, Phys. Rev. E, 74, 3 (2006)

E. Treacy, IEEE J Quant. Elect., 5, 454 (1969)

A. Trisorio, C. P. Hauri, Opt. Lett., 32, 12, 1650 (2007)

S. Tzortzakis, B. Prade, M. Franco, A. Mysyrowicz, Opt. Comm., 181, 1, 123 (2000)

S. Uchida, Y. Shimada, H. Yasuda, S. Motokoshi, C. Yamanaka, T. Yamanaka, Z. Kawasaki, K. Tsubakimoto, J. Opt. Technol. 66, 199 (1999).

S. Varma, Y.-H. Chen, H. M. Milchberg, Phys. Plasmas, 16, 056702 (2009)

S. Varma, Y.-H. Chen, H. M. Milchberg, PRL 101, 205001 (2008)

S. Varma, Y.-H. Chen, J. P. Palastro, A. B. Fallahkair, E. W. Rosenthal, T. Antonsen, H. M. Milchberg, Phys. Rev. A, 86, 023850 (2012)

J. Verdeyen, Laser Electronics, Prentice Hall, 3 (1995)

Th. Vieillard, F. Chaussard, F. Billard, D. Sugny, O. Faucher, S. Ivanov, J.-M. Hartmann, C. Boulet, B. Lavorel, Phy. Rev., 87, 023409 (2013)

D. Walter, S. Eyring, J. Lohbreier, R. Spitzenpfeil, C. Spielmann, App. Phy. B, 88, 175 (2007)

- T.-J. Wang, C. Marceau, Y. Chen, S. Yuan, F. Th'ebberge, M. Ch'ateaneuf, J. Dubois, S. L. Chin,  
Appl. Phys. Lett. 96, 211113 (2010)
- J. Wu, H. Cai, H. Zeng, A. Couairon, Opt. Lett., 33, 2593 (2008)
- J. Wu, H. Cai, H. Zeng, A. Couairon, Phys. Rev. A, 79, 063812 (2009)
- J. Wu, H. Cai, Y. Peng, H. Zeng, Phys. Rev. A 79, 041404 (2009)
- M. Wu, R. J. Bemish, R. E. Miller, J. Chem. Phys. 101, 9447 (1994)
- X. Xie, J.-M. Dai, and X.-C. Zhang, Phys. Rev. Lett. 96, 075005 (2006)
- N. Xu, C. Wu, Y. Gao, H. Jiang, H. Yang, Q. Gong, J. Phys. Chem. A, 112, 612 (2008)
- X. M. Zhao, J. Diels, C. Y. Wang, J. M. Elizondo, IEEE J. Quantum Electron. 31, 599 (1995)